

000 001 002 003 004 005 006 007 008 009 010 011 012 MANIBOX: ENHANCING SPATIAL GRASPING GENERALIZATION VIA SCALABLE SIMULATION DATA GENERATION

013
014
015
016
017
018
019
020
021
022
023
024
025
026
027
028
029
030
Anonymous authors
031
032
Paper under double-blind review

033 034 ABSTRACT

035
036 Learning a precise robotic grasping policy is crucial for embodied agents operating in complex real-world manipulation tasks. Despite significant advancements, most models still struggle with accurate spatial positioning of objects to be grasped. We first show that this spatial generalization challenge stems primarily from the extensive data requirements for adequate spatial understanding. However, collecting such data with real robots is prohibitively expensive, and relying on simulation data often leads to visual generalization gaps upon deployment. To overcome these challenges, we then focus on state-based policy generalization and present **ManiBox**, a novel bounding-box-guided manipulation method built on a simulation-based teacher-student framework. The teacher policy efficiently generates scalable simulation data using bounding boxes, which are proven to uniquely determine the objects' spatial positions. The student policy then utilizes these low-dimensional spatial states to enable zero-shot transfer to real robots. Through comprehensive evaluations in simulated and real-world environments, ManiBox demonstrates a marked improvement in spatial grasping generalization and adaptability to diverse objects and backgrounds. Further, our empirical study into scaling laws for policy performance indicates that spatial volume generalization scales positively with data volume. For a certain level of spatial volume, the success rate of grasping empirically follows Michaelis-Menten kinetics relative to data volume, showing a saturation effect as data increases.¹

037 038 1 INTRODUCTION

039
040 Robotic manipulation in dynamic environments is pivotal for advancing modern robotics (Fu et al., 2024). Equipping robots with precise grasping capabilities in unstructured settings not only extends their utility beyond traditional static scenarios but also enhances their real-world effectiveness, especially in industrial and domestic settings. A robot policy that achieves **spatial generalization**—defined as the ability of a manipulation model to complete tasks regardless of the target object's position within a defined spatial volume—would be particularly practical. Such generalization is vital when deploying robots in diverse environments, such as different households, where they must handle various objects on different platforms. The capability to perform successfully across these varied spatial conditions is essential, as objects in real-world settings are rarely fixed in place, and effective manipulation demands adaptability to a broad range of spatial challenges.

041
042 Recent works have made notable progress in robotic manipulation in multi-task and multi-environment scenarios, which is largely driven by end-to-end training methodologies (Ahn et al., 2022; Shridhar et al., 2022; 2023; Zitkovich et al., 2023). Notably, some large embodied foundation models for manipulation, such as those fine-tuned from Vision-Language Models (VLMs) for multi-task robot manipulation tasks (Brohan et al., 2022; Kim et al., 2024), have made significant strides. However, these large manipulation models derived from VLMs often lack sufficient spatial awareness and reasoning capabilities, posing substantial challenges for large-scale spatial generalization in real-world applications (Cheng et al., 2024a). Our analysis in Lemma 1 suggests that achieving spatial generalization over larger volumes requires substantially more data, a relationship we further empirically verify to follow a positive scaling law (see Figure 4). For example, training a model to

043
044
045
046
047
048
049
050
051
052
053
¹Our data and code are available in the supplementary material.

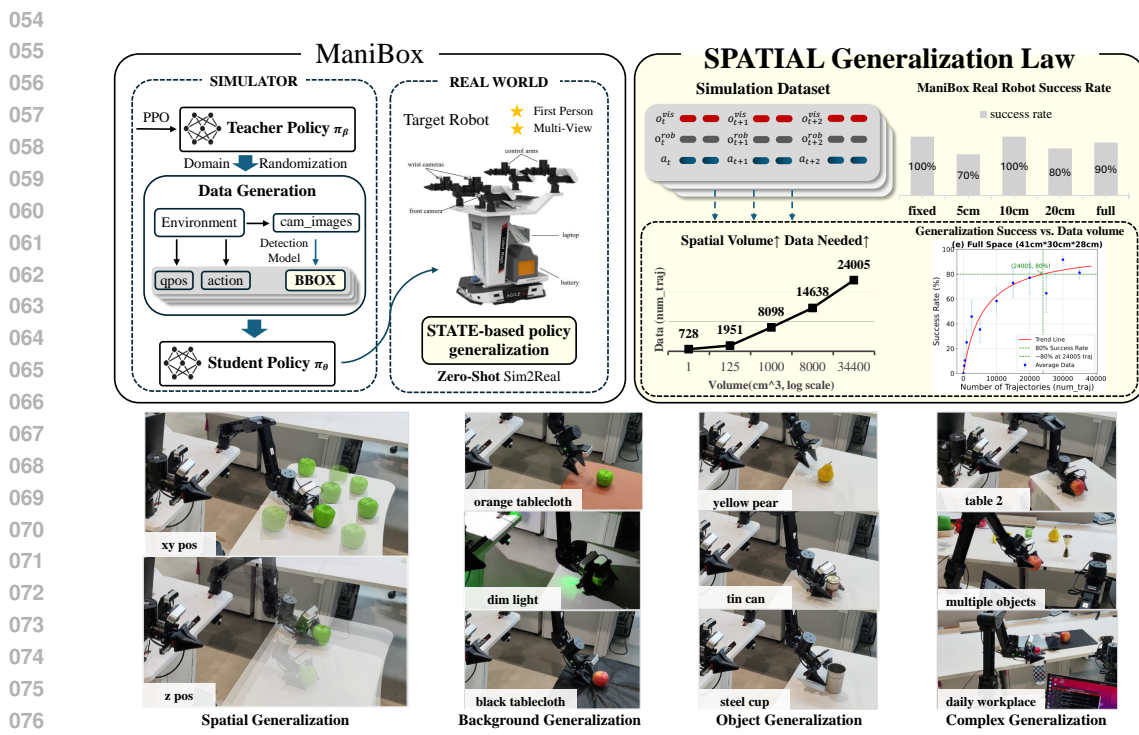


Figure 1: **Overview.** We introduce ManiBox, a bbox-guided manipulation method using a teacher-student framework to enhance spatial generalization in grasping policies. We reveal that spatial volume generalization scales positively with data volume, with grasping success following Michaelis-Menten kinetics relative to data volume for specified spatial volumes. Extensive real-world tests show ManiBox’s robust adaptability to varied spatial positions, objects, and backgrounds.

grasp at a fixed point may require only 50 to 600 trajectory datasets. However, when generalizing the model to operate within a spatial volume of $34,400\text{cm}^3$ ($41\text{cm} \times 30\text{cm} \times 28\text{cm}$), which approximates the maximum reach of our robotic arm, the data requirement increases by roughly 40-fold, demanding tens of thousands of trajectories

However, collecting such a large volume of data on real robots is prohibitively expensive. For instance, RT-1 required 17 months to accumulate 130K episodes (Brohan et al., 2022), which is a level of resource commitment unfeasible for most research labs. Although simulation data can help bridge this gap, significant high-dimensional visual discrepancies between simulated and real environments, known as the Sim2Real gap, pose additional challenges. While prior efforts have aimed to enhance performance using various visual generalization techniques, each method comes with its drawbacks. Some demand unobstructed third-person perspectives (Yuan et al., 2024), some consume substantial computational resources (Shridhar et al., 2023; Ahn et al., 2022). These requirements can impede real-time processing and practical deployment on resource-limited robotic platforms.

While perception models are essential for object and environmental recognition, the true effectiveness of a robot in dynamic settings hinges on the robustness of its policy execution. A well-generalized policy empowers the robot to autonomously adjust its actions in real-time, effectively compensating for visual inaccuracies and adapting to changes in object positions or environmental dynamics. Such adaptability is crucial for achieving task success and maintaining system stability, especially in the face of imperfect or noisy perception data. To further enhance the robot’s ability to manage unpredictable scenarios (e.g. Sec. B.2) and ensure reliable real-world performance, we shift our focus to **state-based policy generalization** instead of relying solely on vision-based methods. Our Lemma 2 demonstrates that bounding boxes, when captured from multiple cameras, effectively encapsulate the 3D structure of convex objects, providing an optimal low-dimensional state for policy generalization. Building on this foundation, we introduce a novel bounding-box-guided methodology **ManiBox** to enhance spatial generalization and adaptability.

In the simulator, ManiBox utilizes reinforcement learning (RL) with privileged information to train a sophisticated teacher policy. This policy generates scalable robot trajectory data, replacing tra-

ditional visual inputs with bounding box coordinates to facilitate spatial generalization of grasping policies. Subsequently, the student policy, trained on this simulation data, achieves robust zero-shot transfer to real-world tasks, leveraging bounding boxes identified by advanced open-vocabulary detection models, such as YOLO-World (Cheng et al., 2024b). Extensive experiments with both simulators and real robots demonstrate a direct correlation between data volume and spatial generalization performance: *more data consistently leads to higher grasping success rates, and generalizing to larger spatial volumes requires even more data*. For instance, to reliably grasp objects within a 1000cm^3 workspace, tens of thousands of trajectories from various positions are required. ManiBox achieves nearly perfect success rates in real-world grasping tasks by leveraging large-scale simulation data generated across diverse spatial volumes. Furthermore, ManiBox exhibits robust generalization, successfully grasping objects in new scenarios, including unfamiliar object types, complex surfaces, changing lighting conditions, and environments with distractions.

Our contributions include: (1) We introduce **ManiBox**, an innovative bounding-box-guided manipulation method that addresses the limitations of visual generalization, offering a robust solution for spatial generalization in grasping tasks; (2) ManiBox significantly enhances adaptability to diverse spatial positions, object types, and backgrounds, as demonstrated by extensive experiments in both simulated and real-world environments; (3) Through scalable simulation data generation, we provide novel insights into the relationship between data volume and spatial generalization, establishing a framework for improving generalization across a variety of embodied systems.

2 RELATED WORK

Learning from Simulation. Simulators provide an efficient and scalable way to expand embodiment datasets, offering a cost-effective means for parallel data collection and faster iteration cycles. There are three main approaches for leveraging simulation in robotic control: 1) training reinforcement learning (RL) agents through interaction within the simulator (Huang et al., 2023; Radosavovic et al., 2024; Yuan et al., 2024), 2) using imitation learning based on expert demonstrations generated in simulation (Xie et al., 2020; Tan et al., 2024), and 3) employing a teacher-student framework, where privileged information from simulation trains a teacher policy to guide a student policy (Lee et al., 2020a; Geng et al., 2023; Zhuang et al., 2023), as demonstrated in the ManiBox framework. These methods reduce the reliance on expensive real-world data collection.

Various techniques have been developed to bridge the Sim2Real gap, including realistic simulators (Todorov et al., 2012; James et al., 2020; Makoviychuk et al., 2021), domain randomization (Tobin et al., 2017; Peng et al., 2018; Zhuang et al., 2023), and vision-based policy generalization (Geng et al., 2023; Tan et al., 2024; Ying et al., 2024; Yuan et al., 2024). These approaches enable robots to generalize across diverse visual and physical conditions, which are critical in real-world environments. For example, domain randomization allows policies trained in varied simulated conditions to transfer effectively to real-world scenarios (Tobin et al., 2017; Peng et al., 2018). While real-world datasets such as Open X-Embodiment (Padalkar et al., 2023) provide 1M demonstrations, they are much smaller than datasets in other domains like language and images (Lehmann et al., 2015; Mühleisen & Bizer, 2012; Weyand et al., 2020; Wu et al., 2019). Thus, simulation-generated datasets play a vital role in compensating for the limitations of real-world data collection.

Visual Generalization for Robotic Manipulation. Visual generalization is fundamental for robotic manipulation in dynamic environments, where robots must handle varying visual inputs and changing conditions, such as object positions and lighting variations. Vision-based policy generalization, which leverages both simulated and real-world data, addresses these challenges. By simulating diverse visual scenarios, robots can better generalize to new environments and tasks. For instance, multi-task and multi-object manipulation studies have extended behavior cloning to handle a wide range of visual inputs, improving generalization to unseen objects and scenes (Vuong et al., 2023; Fang et al., 2023). Additionally, language-conditioned policies (Brohan et al., 2022; Zitkovich et al., 2023; Shridhar et al., 2023) and imitation learning from human videos (Chen et al., 2021; Nair et al., 2023) enable robots to interpret and manipulate objects using both visual and language cues.

However, scaling real-world demonstrations to improve generalization remains challenging due to resource constraints. Simulation-based learning mitigates this by offering large, diverse visual data. Domain randomization techniques (Tobin et al., 2017; Peng et al., 2018) have proven effective in generating varied visual conditions, enabling models to generalize more robustly across real-world

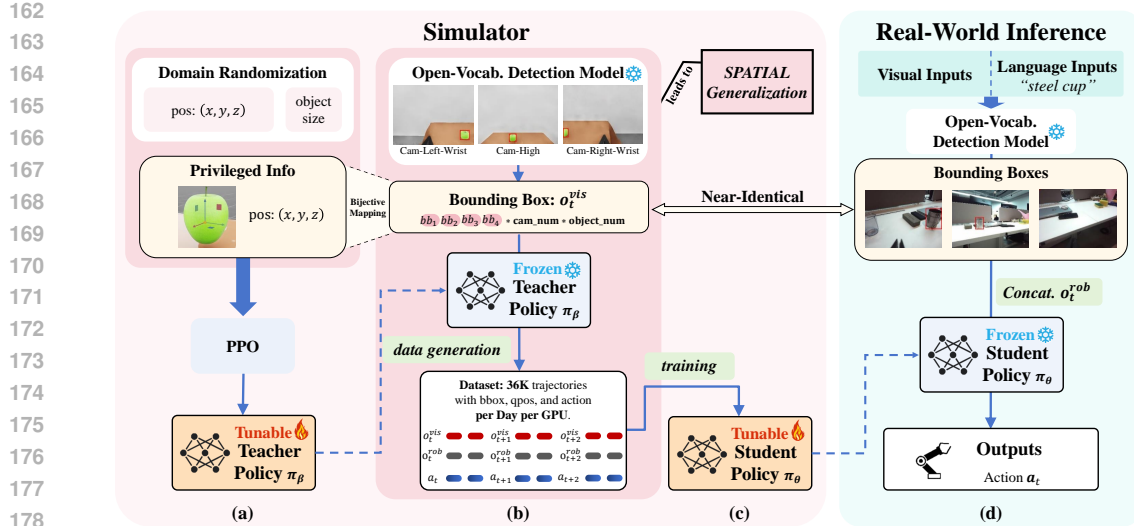


Figure 2: **ManiBox illustration.** (a) Utilizing PPO and domain randomization, we train a sophisticated teacher policy in the simulator that utilizes privileged object information to determine actions. (b) The teacher policy generates scalable trajectory data, utilizing bounding box coordinates instead of traditional high-dimensional visual inputs or privileged information. (c) A state-based student policy, generalizable and capable of zero-shot transfer, is trained on this extensive simulation dataset, greatly improving spatial generalization. (d) Guided by bounding boxes, the student policy precisely executes actions for real robots, achieving improved generalization capabilities.

tasks. While methods like bounding box annotations assist in specific tasks such as pose estimation (Huang et al., 2023), understanding the relationship between dataset scale and generalization remains an area that requires further exploration. As simulation data grows, more research is needed to evaluate how data volume impacts policy generalization, particularly in dynamic environments.

3 METHODOLOGY

In this section, we first formulate the problem and then introduce our method ManiBox, including the teacher policy training, simulation data generalization, and student policy distillation.

3.1 PROBLEM FORMULATION

For robotic manipulation, especially within dynamic environments, achieving spatial generalization (i.e., the ability to effectively perform tasks across varied spatial configurations) is essential for usability and overall efficacy. We formulate robotic manipulation as a partially observable Markov decision process (POMDP) (Cassandra et al., 1994), by considering the robot’s limited access to complete state information, the necessity to make decisions under uncertainty, as well as the inherently stochastic nature of its interactions with the environment. Formally, the decision-making process is characterized by the tuple $\mathcal{M} = (\mathcal{S}, \mathcal{A}, \mathcal{O}, \mathcal{T}, \mathcal{R}, \gamma)$, where \mathcal{S} represents the state space, including all configurations of the robot and its environment; \mathcal{A} denotes the action space, containing all possible robot actions; \mathcal{O} is the observation space, which reflects the limited state information accessible to the robot; \mathcal{T} defines the state transition dynamics, $\mathcal{T}(s_{t+1}|s_t, a_t)$; \mathcal{R} is the reward function, providing feedback based on the state-action pair $\mathcal{R}(s_t, a_t)$; and γ is the discount factor.

In real-world scenarios, the robot receives partial observations $o_t \in \mathcal{O}$ through an observation function, which provides incomplete and potentially noisy information about the true state s_t . The observation can be represented as $o_t \sim \mathcal{O}(s_t)$. The robot’s objective is to find a policy π that maps observations (or histories of observations) to actions $a_t \sim \pi(a_t | \tau_t)$, where $\tau_t = (o_0, a_0, o_1, a_1, \dots, o_t)$ is the history up to time t . The policy is expected to maximize the expected cumulative reward:

$$J(\pi) = \mathbb{E}_\pi \left[\sum_{t=0}^{\infty} \gamma^t \mathcal{R}(s_t, a_t) \right], \quad (1)$$

where the expectation is over the trajectories induced by the policy π . However, solving POMDPs for manipulation tasks is computationally expensive, as it requires maintaining a belief distribution

over all possible states, including the precise position, orientation, and object dynamics. This complexity is compounded by the need to handle occlusions, sensor noise, and dynamic changes in the environment, making it challenging for robots to operate efficiently in real-world settings where the state is constantly evolving and uncertain (Kaelbling et al., 1998; Kochenderfer, 2015).

To reduce this complexity and ensure Sim2Real transfer, we adopt a widely used teacher-student framework (Lee et al., 2020a; Geng et al., 2023), building upon which, we develop **ManiBox**, a novel bounding-box-guided manipulation method that offers significant advantages in spatial generalization over vision-based RL methods. First, ManiBox enables efficient, scalable data generation, as the teacher policy in simulation can produce a large and diverse set of trajectories. Additionally, by using low-dimensional bounding box states, the state-based student policy can accelerate learning and effectively transfer from simulation to the real world.

However, this framework also faces notable challenges. The teacher policy must efficiently explore a high-dimensional state space in simulation, which can be computationally intensive. The student policy must derive optimal actions from incomplete observations and adjust to real-world variations such as sensor noise and dynamic environmental conditions not present in simulations. Detailed strategies for overcoming these challenges are discussed in the following sections.

3.2 TEACHER POLICY TRAINING

To automatically and efficiently generate a large amounts of diverse data, we first train an expert teacher policy $\pi_\beta : \mathcal{S} \rightarrow \mathcal{A}$ using RL, as the expert data generator. The **teacher policy** $\pi_\beta(a_t | s_t)$ is trained in a simulated environment where it has access to full state information s_t , including privileged information such as precise object positions. The teacher policy is optimized using reinforcement learning (RL) to maximize the expected reward:

$$J_\beta = \mathbb{E}_{\pi_\beta} \left[\sum_{t=0}^{\infty} \gamma^t \mathcal{R}(s_t, a_t) \right], \quad (2)$$

where the reward function is defined to guide the policy in grasping the object and moving it to a specified location. We select the grasping task to validate our approach’s core concept. This allows the teacher to generate a diverse set of optimal trajectories across a wide range of spatial configurations. These trajectories serve as training data for the student policy, guiding it to learn effective manipulation policies.

The advantages of state-based teacher policies lie in their lower-dimensional states, enabling more efficient learning, reduced exploration space through privileged information, and support for larger parallel environments. To leverage these benefits, in addition to optimizing the policy using the Proximal Policy Optimization (PPO) (Schulman et al., 2017) algorithm, we make adjustments to the RL environment to reduce the exploration space and make it easier for the policy π_β to find the point with the highest return. Moreover, to support follow-up Sim2Real and spatial generalization, we carefully design the environment below (More details are in Appendix E.1):

Environment Setup. To ensure efficient data generation and policy training, we utilize Isaac Lab (Mittal et al., 2023), which supports large-scale parallelism environments. The scene includes basic elements like a platform, objects, and a robot, arranged simply to facilitate future domain randomization. The robot’s goal is to grasp the object on the table and move it to a designated location. We integrate the dual-arm Mobile ALOHA (Fu et al., 2024) robot, equipped with three first-person view RGB cameras, into the simulator and ensure its dynamics are consistent with the real world.

State. For training efficiency, our teacher policy is state-based and can access full state information s_t . As the robot lacks visual input, we include privileged information like the object’s position in the state information. The privileged information accelerates RL training and enables the agent to learn more efficient and generalized policies.

Domain Randomization. To improve the generalization of the teacher policy and enhance the spatial diversity of the generated data, we adopt several domain randomization techniques:

- *objective position* (x, y, z): To generalize the grasping policy to the whole space, we apply the domain randomization for all three dimensions of x , y , and z , ensuring that the x -coordinate and y -coordinate of the object, which is chosen randomly, can cover a large range. Moreover, the height of the platform is randomized to ensure that the z -coordinate of the object in the data can cover the feasible working space of the robotic arm.

- 270 • *object size*: To ensure that the grasping policy covers objects of *various sizes*, the size of
 271 the object is also randomized.

272 These two domain randomization techniques allow teacher policy can grasp different objects of
 273 different positions and sizes, which is significant for real-world generalization. By combining privi-
 274 leged information and domain randomization, the teacher policy can efficiently generate a large
 275 amount of diverse data to achieve spatial generalization.

277 3.3 SIMULATION DATA GENERATION

279 We utilize the teacher policy to automatically generate data for training a student policy that can be
 280 deployed in the real world across different objects, grasping spatial positions, and backgrounds.

281 **Data Volume Estimation.** To guide the data volume needed for policy generalization to a specific
 282 spatial volume, we now analyze the sample efficiency for generalizing in a $b \times b \times b$ cube. Based on
 283 the classical learning theory, the sample complexity of uniform convergence property is in proportion
 284 to the VC dimension of the model hypothesis set (Shalev-Shwartz & Ben-David, 2014). Extending
 285 previous results about generalization bounds for multi-task learning (Crammer & Mansour, 2012),
 286 we can have the following results:

287 **Lemma 1** (Details are in Appendix A.1). *For training a grasp agent that can generalize spatially
 288 within a cube whose size is $b \times b \times b$ via imitation learning, under some mild assumptions in Crammer
 289 & Mansour (2012), the VC dimension is at most proportional to $d \log(Cb^3d)$, where d is the VC
 290 dimension of the hypothesis set for grasping the fixed point and C is a constant independent of d, b .*

291 This lemma demonstrates that the data required for policy generalization to a certain volume grows,
 292 thus it is necessary to collect data from the simulator. This result gives us a rough estimation of how
 293 much data we need to collect with the increasing of the spatial cube needs to generalize.

295 In light of this Lemma 1, we need a large scale of trajectories to train a student policy feasible
 296 under full spatial range. This calls for conciseness in data generation and collection, otherwise it
 297 will place a heavy burden on student policy training. On the other hand, since the teacher policy
 298 trained with privileged information (i.e. object positions) cannot directly transfer from simulation
 299 to reality (Sim2Real), the student policy needs visual observations that implicitly encode object
 300 position information. However, there remains a significant Sim2Real gap between visual images in
 301 the simulator and those in the real world because the vast complexity of real-world environments
 302 cannot be fully simulated by the simulator (e.g. various backgrounds and objects). Additionally,
 303 vision-based policy is difficult to train on a large scale and requires data augmentation.

304 To address this Sim2Real gap and enable robust spatial generalization, we propose using an individ-
 305 ual vision module to extract the bounding box from camera views as a **consistent, low-dimensional,**
 306 **and complete** representation of the object’s spatial properties, such as position and size.

307 **Using Bounding Boxes to Provide Complete 3D Information about the Object.** To efficiently
 308 generate a large amount of simulator data that aligns with real-world visual images, the vision mod-
 309 ule must be robust, mature, and efficient. Considering open-vocabulary detection, we selected
 310 YOLO-World (Cheng et al., 2024b) as the frozen 2D visual feature extraction module. This pro-
 311 vides us with the bounding box of the objects as the 2D low-dimensional visual feature, which is
 312 consistent and low-dimensional. Notably, the inference time of YOLO-World for a single image is
 313 around 30ms , ensuring the data generalization efficiency and real-time inference in the real world.

314 In addition, to ensure that these multi-view 2D low-dimensional visual features can offer complete
 315 information about object position and size, we present a lemma: Suppose the object is a sphere, the
 316 3D information of the object can be uniquely determined by the bounding boxes from two cameras:

317 **Lemma 2** (Details and proofs are in Appendix A.2). *Given: (1) Two pinhole cameras with known
 318 intrinsic parameters K_i and extrinsic parameters (R_i, t_i) ; (2) A sphere of unknown radius r is fully
 319 visible in both camera images without occlusion; (3) Normalized image coordinates of the bounding
 320 boxes of the sphere in both images: Camera i : $(u_{1min}, v_{1min}, u_{1max}, v_{1max})$, the image dimensions are
 321 known (width W_i and height H_i for each camera).*

322 *Then the 3D coordinates of the sphere’s center C in the world coordinate system and the radius r
 323 of the sphere can be uniquely determined using the known camera parameters, and the normalized
 324 bounding box coordinates, provided that the cameras are not in degenerate configurations.*

This lemma illustrates that 3D position information of a sphere can be implied by utilizing multi-view bounding boxes (Hartley & Zisserman, 2003), indicating our ManiBox can capture complete spatial position information of target objects for real-world control policies.

In short, our approach of using an individual vision module simplifies the transition from simulation to the real world by providing the student policy with consistent inputs across both domains. Specifically, the student policy receives both proprioceptive data $\mathcal{O}_t^{\text{rob}}$ and bounding box data $\mathcal{O}_t^{\text{vis}}$ as inputs:

$$\pi_\theta : \mathcal{O} = \mathcal{O}_{\text{rob}} \times \mathcal{O}_{\text{vis}} \rightarrow \mathcal{A}. \quad (3)$$

3.4 STUDENT POLICY DISTILLATION

While the teacher policy and data generation are completed in the simulator, the student policy is deployed on a real robot and relies only on partial observations in the real world. The student policy needs to ensure high generalizability in real-world environments. Consequently, real-world variations, such as sensor noise and dynamic environments, pose challenges not encountered in the simulation environment to our student policy. For instance, an open-vocabulary detection model(namely YOLO-World (Cheng et al., 2024b) in our practice) can fail to recognize real-world target objects at times because of background distraction or robot gripper occlusion, while the recognition of the simulated target object rarely fails.

In this context, we introduce the random mask to bridge this sim-to-real gap and further improve the robustness of our policy. In detail, when distilling our student policy from the simulation data \mathcal{D} , for each trajectory, we randomly mask some bboxes(i.e., set them to 0) with a probability pre-defined as `random_mask_ratio`, indicating that this camera does not recognize the target object. This approach replicates the real-world scenarios where the open-vocabulary detection model fails to generate the bounding box.

On top of this expected unpredictable failure and partial observability, our policy requires encoding sufficient history information (Hafner et al., 2019; Lee et al., 2020b; Ying et al., 2023). For this reason, we use RNN for our student policy:

$$\begin{aligned} \mathbf{x}_t, \mathbf{h}_t &= \text{LSTM}(\mathbf{s}'_t, \mathbf{h}_{t-1}), \\ \mathbf{a}_t &= \text{FC}_2(\text{drop}(\text{gelu}(\text{FC}_1(\mathbf{x}_t)))), \end{aligned} \quad (4)$$

where \mathbf{s}'_t and \mathbf{h}_t denotes the input state and the hidden state of the LSTM at time t , \mathbf{x}_t is the intermediate output of the LSTM, and \mathbf{a}_t is the action vector output by the policy. Furthermore, $\text{LSTM}(\cdot)$, $\text{gelu}(\cdot)$, $\text{drop}(\cdot)$, $\text{FC}(\cdot)$ represent the Long Short-Term Memory (LSTM) (Hochreiter & Schmidhuber, 1997), Gaussian Error Linear Unit (GELU) activation (Hendrycks & Gimpel, 2016), dropout (Srivastava et al., 2014), and Fully Connected layer (FC) respectively.

This combination of random mask and trajectory modeling significantly contributes to the robustness and generalization of our student policy in deployment, conquering the challenge of partial observations and unseen real-world variations. (More Sim2Real techniques in Appendix E.4)

4 EXPERIMENTS

In this section, we conduct extensive experiments in both the simulator and the real world, covering various random backgrounds, objects, and positions to answer the following questions: (1) What is the scaling relationship between spatial generalization and data amounts in the grasping task? (Sec. 4.2) and (2) What about the efficacy of our method, especially its generalization ability to different backgrounds, objects, and object spatial positions in real-world applications? (Sec. 4.3)

4.1 EXPERIMENTAL SETUP

Tasks. To validate the generalization of Manibox, we test our approach under the grasping task. In the simulator, the articulated arm and end effector are required to pick up a green apple randomly placed on a table in a $41\text{cm} * 30\text{cm} * 28\text{cm}$ (length*width*height) spatial scale, which is referred to as "Full Space." Also, real-world counterparts are established with alternative objects, backgrounds, and settings to further demonstrate the generalization ability. In both scenarios, three RGB images taken by wrist cameras and the exterior camera are taken as observations.

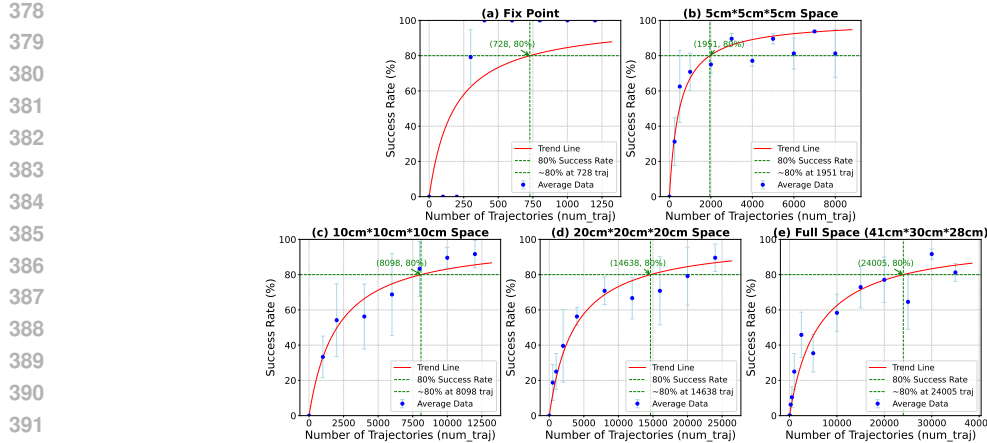


Figure 3: The scaling relationship between spatial generalization and data volume in the grasping task, measured under different spatial ranges. Data volume represents the number of trajectories used to train the student policy. The estimated 80% success point is marked, with blue points showing the average success rate across three seeds and error bars indicating standard deviation.

Real Robot. Mobile ALOHA (Fu et al., 2024) is a cost-effective and highly stable robot designed for both data collection and manipulation tasks. It owns four arms: two for teleoperation during data collection and two subordinate arms that perform manipulation tasks. Each subordinate arm is fitted with an RGB camera on its wrist, complemented by another RGB camera centrally mounted on the robot’s body. Mobile ALOHA has demonstrated strong generalization capabilities across a diverse range of complex grasping tasks, making it an ideal choice for implementing our student policy.

4.2 SPATIAL SCALING LAW WITH DATA

To guide us in determining the data volume required for a certain level of spatial generalization, we investigate the relationship between policy performance and data volume. We conduct extensive experiments in the simulator to evaluate the success rate of policies trained on different data volumes. We select five distinct spatial ranges to explore this scaling behavior, including one fixed range and four dynamic ranges of 5, 10, 20 units, and full space. For each spatial range, we select more than 8 data volumes to train the student policy and evaluate its grasping success rate at random positions.

The results shown in Fig. 3 demonstrate that a scaling law holds in this context: For each spatial range, the pattern is as follows: when the data volume is zero, the policy inevitably fails. As the data volume increases, the success rate of the grasping policy improves, but the growth slows down. Eventually, the success rate surpasses 80% and tends to 100%.

Furthermore, we identify the data volume required to achieve an 80% success rate for each spatial range (as shown in Fig. 3) and find that the volume of the spatial range and the required data follow a power rate relationship (as shown in Fig. 4). The positive correlation between data volume and spatial volume provides guidance for data-driven spatial generalization: The more data we have, the higher the robot’s manipulation success rate. As the spatial range increases, more data is required, and the data volume needed grows with the space volume as a power rate relationship. In fact, for the same task, achieving high generalization success over a $41cm * 30cm * 28cm = 34440cm^3$ range may require at least 20,000 trajectory data from different spatial positions. Such large-scale data collection would be expensive in the real world, making simulator-generated data a more affordable and efficient option. This further emphasizes the significance of simulation data.

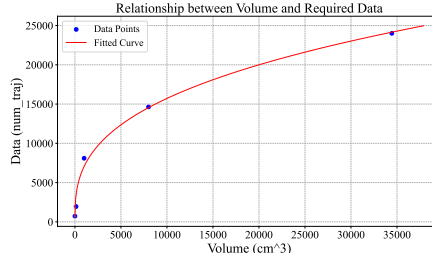


Figure 4: The relationship between spatial volume and data amounts needed to reach 80% grasping success rate. The fitted curve represents a power function $y = 640.32 \cdot x^{0.35}$.

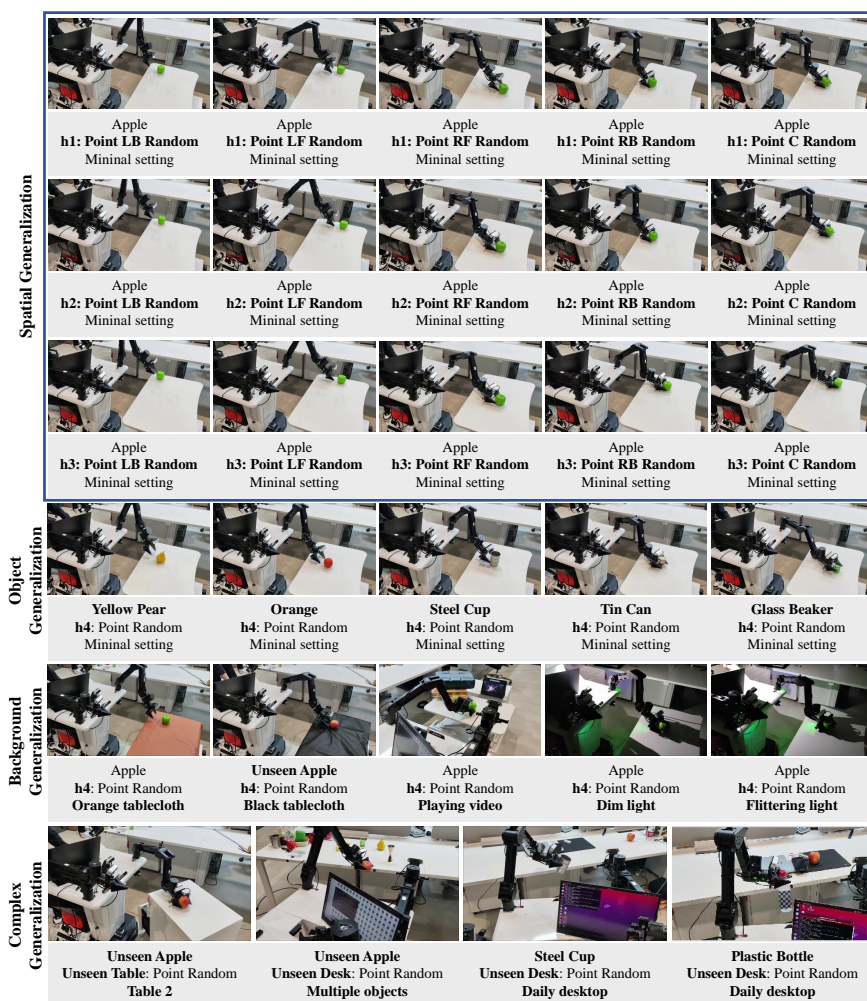


Figure 5: Demonstration of the generalization of our methods across different backgrounds, objects, and positions. The h_1 , h_2 , h_3 , h_4 are randomly selected object heights in the real world, which are approximately 57cm, 65cm, 72cm, and 65cm. LB, LF, RF, RB, and C are abbreviations for Left-Back, Left-Front, Right-Front, Right-Back, and Center area respectively.

To further demonstrate the importance of other variables (e.g. time) in spatial intelligence and the robustness of policy generalization to visual uncertainty, we have further discussion on the spatial intelligence of our policy through detailed ablation experiments. Details are provided in Appendix B.

4.3 REAL-WORLD RESULTS

To validate the generalization ability of our method and policy in the real world, we compare the success rate of our policy with the vision-based ACT. In practice, we deploy models trained on simulation data onto a real robot and test their performance on grasping tasks across multiple arbitrarily chosen positions, eight objects (with some of them out-of-distribution), five backgrounds, and three complex settings as illustrated in Figure 5. [More tasks, pictures, and videos of the experiment are available in the Appendix C](#) and supplementary materials. More experiment details of these tests are in the Appendix D.3.

Spatial generalization. To justify the efficacy of our method, we assess the generalization capability of our student policy across four spatial ranges and a fixed point. For each experiment, we randomly place an apple, different from its counterpart in the simulator in both shape and material, on the table at arbitrarily chosen heights within the given range (as illustrated in the first three rows of Fig. 5). Alongside the difference in form and appearance, the apple presents considerable

unpredictability to the visual detection model due to factors including background, lighting, target object, etc. Consequently, the bounding box varies in size or even disappears at times, emphasizing the need for robustness in the policy. As shown in Tab. 1, our policy generalizes well to objects falling in different spatial volumes, achieving a success rate between 70% and 100%. In contrast, vision-based ACT, which trains the student policy with the vision input ACT (Zhao et al., 2023) on video-action simulation data, experiences a visible drop on success rate when spatial range scales up, despite its considerable success rate of 70% on a fixed point. The wanting performance of the baseline further demonstrates the significance and necessity of exploring spatial generalization. The results demonstrate that our method harbors strong generalization when addressing uncertainties arising from real-world objects, variations in spatial positions, and visual detection interferences.

Object generalization. In addition, to justify the object generalization ability of our method, we test our model across eight objects including original apple, unseen apple, yellow pear, orange, steel cup, tin can, glass beaker, and plastic bottle at arbitrarily selected positions. For each unseen object, feeding the corresponding name as a supplement into

the open-vocabulary visual detection model is enough for the policy to grasp the target object. Tab. 4 shows detailed object size information for training and inference. It is worth noting that five of the selected objects are out-of-distribution in size (their bounding box sizes are unseen in the simulation data) in an attempt to further illustrate the object generalization ability of our method. This certain level of generalization observed, even when there is significant variation in the bounding box, aligns with our Lemma 2, which proves that the 3D position information of the object is complete in the dataset.

Background Generalization. Utilizing the open-vocab detection ability of YOLO-World, ManiBox can handle various backgrounds and vision disruptions without intentionally varied visual domain randomization. To verify this ability, we experiment with tables of three different shapes and tablecloths in two colors under the minimal setting of a table, an object, and a robot. In addition, we alter the lighting conditions by employing a single stationary point light source and a single flickering point light, as well as playing videos in the background as distractions. Furthermore, we construct two more complex scenarios, one representing a multi-object environment and the other replicating a typical daily workplace desktop. The results demonstrate the strong background generalization ability of our policy. Even though the visual detection model occasionally makes mistakes, the generalization of our policy compensates for those errors. This can be attributed to our policy’s endeavor to integrate historical information and random masking to increase the visual model’s tolerance for errors. Arguments for them can be found in Appendix B.

5 CONCLUSION

In this work, we present ManiBox, a novel bbox-guided manipulation method, using a simulation-based teacher-student framework to enhance the spatial generalization of grasping policies. To address the challenge of the generalization gap in vision-based models from simulation to real-world deployment, we propose a generalizable, state-based student policy that is innovatively equipped with bbox positions. This policy is trained on scalable simulation data generated by the teacher policy. Extensive experiments in both simulated and real-world environments demonstrate that ManiBox significantly outperforms existing methods in adapting to diverse spatial positions, object configurations, and background variations. Moreover, our theoretical and empirical analyses reveal that the generalization of spatial volume scales positively with the data volume, and the success rate follows Michaelis-Menten kinetics for specified spatial volumes. These findings pave the way for the development of robust spatial generalization across a wide range of embodied systems.

Table 1: The real-world success rate of our method and vision-based ACT under varied spatial volumes. We select an approximate data amount based on the results in Fig. 3.

Spatial Range	Methods	Success Rate
Fix Point	Vision-Based ACT	70%
	ManiBox (Ours)	100%
5cm*5cm*5cm	Vision-Based ACT	0%
	ManiBox (Ours)	70%
10cm*10cm*10cm	Vision-Based ACT	0%
	ManiBox (Ours)	100%
20cm*20cm*20cm	Vision-Based ACT	-
	ManiBox (Ours)	80%
Full Space (41cm*30cm*28cm)	Vision-Based ACT	-
	ManiBox (Ours)	90%

540 REFERENCES
541

- 542 Michael Ahn, Anthony Brohan, Noah Brown, Yevgen Chebotar, Omar Cortes, Byron David, Chelsea
543 Finn, Chuyuan Fu, Keerthana Gopalakrishnan, Karol Hausman, et al. Do as i can, not as i say:
544 Grounding language in robotic affordances. *arXiv preprint arXiv:2204.01691*, 2022.
- 545 Anthony Brohan, Noah Brown, Justice Carbajal, Yevgen Chebotar, Joseph Dabis, Chelsea Finn,
546 Keerthana Gopalakrishnan, Karol Hausman, Alex Herzog, Jasmine Hsu, et al. Rt-1: Robotics
547 transformer for real-world control at scale. *arXiv preprint arXiv:2212.06817*, 2022.
- 548 Anthony R Cassandra, Leslie Pack Kaelbling, and Michael L Littman. Acting optimally in partially
549 observable stochastic domains. In *Aaaai*, volume 94, pp. 1023–1028, 1994.
- 550 Annie S Chen, Suraj Nair, and Chelsea Finn. Learning generalizable robotic reward functions from “
551 in-the-wild” human videos. *arXiv preprint arXiv:2103.16817*, 2021.
- 552 An-Chieh Cheng, Hongxu Yin, Yang Fu, Qiushan Guo, Ruihan Yang, Jan Kautz, Xiaolong Wang,
553 and Sifei Liu. Spatialrgpt: Grounded spatial reasoning in vision language model, 2024a. URL
554 <https://arxiv.org/abs/2406.01584>.
- 555 Tianheng Cheng, Lin Song, Yixiao Ge, Wenyu Liu, Xinggang Wang, and Ying Shan. Yolo-world:
556 Real-time open-vocabulary object detection. In *Proceedings of the IEEE/CVF Conference on
557 Computer Vision and Pattern Recognition*, pp. 16901–16911, 2024b.
- 558 Koby Crammer and Yishay Mansour. Learning multiple tasks using shared hypotheses. *Advances
559 in Neural Information Processing Systems*, 25, 2012.
- 560 Hao-Shu Fang, Chenxi Wang, Hongjie Fang, Minghao Gou, Jirong Liu, Hengxu Yan, Wenhui Liu,
561 Yichen Xie, and Cewu Lu. Anygrasp: Robust and efficient grasp perception in spatial and tem-
562 poral domains. *IEEE Transactions on Robotics*, 2023.
- 563 Zipeng Fu, Tony Z Zhao, and Chelsea Finn. Mobile aloha: Learning bimanual mobile manipulation
564 with low-cost whole-body teleoperation. *arXiv preprint arXiv:2401.02117*, 2024.
- 565 Haoran Geng, Ziming Li, Yiran Geng, Jiayi Chen, Hao Dong, and He Wang. Partmanip: Learning
566 cross-category generalizable part manipulation policy from point cloud observations. In *Proceed-
567 ings of the IEEE/CVF Conference on Computer Vision and Pattern Recognition*, pp. 2978–2988,
568 2023.
- 569 Danijar Hafner, Timothy Lillicrap, Jimmy Ba, and Mohammad Norouzi. Dream to control: Learning
570 behaviors by latent imagination. *arXiv preprint arXiv:1912.01603*, 2019.
- 571 Richard Hartley and Andrew Zisserman. *Multiple view geometry in computer vision*. Cambridge
572 university press, 2003.
- 573 Sepp Hochreiter and Jürgen Schmidhuber. Long short-term memory. *Neural Computation*, 9(8):
574 1735–1780, 1997.
- 575 Baichuan Huang, Jingjin Yu, and Siddarth Jain. Earl: Eye-on-hand reinforcement learner for dy-
576 namic grasping with active pose estimation. In *2023 IEEE/RSJ International Conference on
577 Intelligent Robots and Systems (IROS)*, pp. 2963–2970. IEEE, 2023.
- 578 Stephen James, Zicong Ma, David Rovick Arrojo, and Edward Johns. Rlbench: The robot learning
579 benchmark & learning environment. *IEEE Robotics and Automation Letters (RA-L)*, 5(2):3019–
580 3026, 2020.
- 581 Leslie Pack Kaelbling, Michael L Littman, and Anthony R Cassandra. Planning and acting in
582 partially observable stochastic domains. *Artificial intelligence*, 101(1-2):99–134, 1998.
- 583 Moo Jin Kim, Karl Pertsch, Siddharth Karamcheti, Ted Xiao, Ashwin Balakrishna, Suraj Nair,
584 Rafael Rafailov, Ethan Foster, Grace Lam, Pannag Sanketi, et al. Openvla: An open-source
585 vision-language-action model. *arXiv preprint arXiv:2406.09246*, 2024.

- 594 Mykel J Kochenderfer. *Decision making under uncertainty: theory and application*. MIT press,
 595 2015.
- 596
- 597 Joonho Lee, Jemin Hwangbo, Lorenz Wellhausen, Vladlen Koltun, and Marco Hutter. Learning
 598 quadrupedal locomotion over challenging terrain. *Science robotics*, 5(47):eabc5986, 2020a.
- 599 Kimin Lee, Younggyo Seo, Seunghyun Lee, Honglak Lee, and Jinwoo Shin. Context-aware dynam-
 600 ics model for generalization in model-based reinforcement learning. In *International Conference
 601 on Machine Learning*, pp. 5757–5766. PMLR, 2020b.
- 602
- 603 Jens Lehmann, Robert Isele, Max Jakob, Anja Jentzsch, Dimitris Kontokostas, Pablo N Mendes,
 604 Sebastian Hellmann, Mohamed Morsey, Patrick Van Kleef, Sören Auer, et al. Dbpedia—a large-
 605 scale, multilingual knowledge base extracted from wikipedia. *Semantic web*, 6(2):167–195, 2015.
- 606 Shilong Liu, Zhaoyang Zeng, Tianhe Ren, Feng Li, Hao Zhang, Jie Yang, Chunyuan Li, Jianwei
 607 Yang, Hang Su, Jun Zhu, et al. Grounding dino: Marrying dino with grounded pre-training for
 608 open-set object detection. *arXiv preprint arXiv:2303.05499*, 2023.
- 609
- 610 Wolfgang Maass. Neural nets with superlinear vc-dimension. *Neural Computation*, 6(5):877–884,
 611 1994.
- 612 Viktor Makovychuk, Lukasz Wawrzyniak, Yunrong Guo, Michelle Lu, Kier Storey, Miles Macklin,
 613 David Hoeller, Nikita Rudin, Arthur Allshire, Ankur Handa, et al. Isaac gym: High performance
 614 gpu-based physics simulation for robot learning. *arXiv preprint arXiv:2108.10470*, 2021.
- 615
- 616 Leonor Michaelis, Maud L Menten, et al. Die kinetik der invertinwirkung. *Biochem. z.*, 49(333-369):
 617 352, 1913.
- 618 Mayank Mittal, Calvin Yu, Qinxi Yu, Jingzhou Liu, Nikita Rudin, David Hoeller, Jia Lin Yuan,
 619 Ritvik Singh, Yunrong Guo, Hammad Mazhar, et al. Orbit: A unified simulation framework for
 620 interactive robot learning environments. *IEEE Robotics and Automation Letters*, 8(6):3740–3747,
 621 2023.
- 622
- 623 Hannes Mühleisen and Christian Bizer. Web data commons-extracting structured data from two
 624 large web corpora. *LDOW*, 937(133-145):65, 2012.
- 625
- 626 Suraj Nair, Aravind Rajeswaran, Vikash Kumar, Chelsea Finn, and Abhinav Gupta. R3m: A univer-
 627 sal visual representation for robot manipulation. In *Conference on Robot Learning*, pp. 892–909.
 628 PMLR, 2023.
- 629
- 630 Abhishek Padalkar, Acorn Pooley, Ajinkya Jain, Alex Bewley, Alex Herzog, Alex Irpan, Alexander
 631 Khazatsky, Anant Rai, Anikait Singh, Anthony Brohan, et al. Open x-embodiment: Robotic
 632 learning datasets and rt-x models. *arXiv preprint arXiv:2310.08864*, 2023.
- 633
- 634 Xue Bin Peng, Marcin Andrychowicz, Wojciech Zaremba, and Pieter Abbeel. Sim-to-real transfer of
 635 robotic control with dynamics randomization. In *2018 IEEE international conference on robotics
 636 and automation (ICRA)*, pp. 3803–3810. IEEE, 2018.
- 637
- 638 Ilija Radosavovic, Tete Xiao, Bike Zhang, Trevor Darrell, Jitendra Malik, and Koushil Sreenath.
 639 Real-world humanoid locomotion with reinforcement learning. *Science Robotics*, 9(89):eadl9579,
 640 2024.
- 641
- 642 John Schulman, Filip Wolski, Prafulla Dhariwal, Alec Radford, and Oleg Klimov. Proximal policy
 643 optimization algorithms. *arXiv preprint arXiv:1707.06347*, 2017.
- 644
- 645 Shai Shalev-Shwartz and Shai Ben-David. *Understanding machine learning: From theory to algo-
 646 rithms*. Cambridge university press, 2014.
- 647
- 648 Mohit Shridhar, Lucas Manuelli, and Dieter Fox. Cliport: What and where pathways for robotic
 649 manipulation. In *Conference on robot learning*, pp. 894–906. PMLR, 2022.
- 650
- 651 Mohit Shridhar, Lucas Manuelli, and Dieter Fox. Perceiver-actor: A multi-task transformer for
 652 robotic manipulation. In *Conference on Robot Learning*, pp. 785–799. PMLR, 2023.

- 648 Eduardo D Sontag et al. Vc dimension of neural networks. *NATO ASI Series F Computer and*
 649 *Systems Sciences*, 168:69–96, 1998.
- 650
 651 Nitish Srivastava, Geoffrey Hinton, Alex Krizhevsky, Ilya Sutskever, and Ruslan Salakhutdinov.
 652 Dropout: a simple way to prevent neural networks from overfitting. *The journal of machine*
 653 *learning research*, 15(1):1929–1958, 2014.
- 654 Hengkai Tan, Songming Liu, Kai Ma, Chengyang Ying, Xingxing Zhang, Hang Su, and Jun Zhu.
 655 Fourier controller networks for real-time decision-making in embodied learning. In *Forty-first*
 656 *International Conference on Machine Learning*, 2024. URL [https://openreview.net/](https://openreview.net/forum?id=nDps3Q8j21)
 657 [forum?id=nDps3Q8j21](https://openreview.net/forum?id=nDps3Q8j21).
- 658
 659 Josh Tobin, Rachel Fong, Alex Ray, Jonas Schneider, Wojciech Zaremba, and Pieter Abbeel. Do-
 660 main randomization for transferring deep neural networks from simulation to the real world. In
 661 *2017 IEEE/RSJ international conference on intelligent robots and systems (IROS)*, pp. 23–30.
 662 IEEE, 2017.
- 663 Emanuel Todorov, Tom Erez, and Yuval Tassa. Mujoco: A physics engine for model-based control.
 664 In *2012 IEEE/RSJ international conference on intelligent robots and systems*, pp. 5026–5033.
 665 IEEE, 2012.
- 666 An Dinh Vuong, Minh Nhat Vu, Hieu Le, Baoru Huang, Binh Huynh, Thieu Vo, Andreas Kugi, and
 667 Anh Nguyen. Grasp-anything: Large-scale grasp dataset from foundation models. *arXiv preprint*
 668 *arXiv:2309.09818*, 2023.
- 669
 670 Tobias Weyand, Andre Araujo, Bingyi Cao, and Jack Sim. Google landmarks dataset v2-a large-
 671 scale benchmark for instance-level recognition and retrieval. In *Proceedings of the IEEE/CVF*
 672 *conference on computer vision and pattern recognition*, pp. 2575–2584, 2020.
- 673 Baoyuan Wu, Weidong Chen, Yanbo Fan, Yong Zhang, Jinlong Hou, Jie Liu, and Tong Zhang.
 674 Tencent ml-images: A large-scale multi-label image database for visual representation learning.
 675 *IEEE access*, 7:172683–172693, 2019.
- 676
 677 Fan Xie, Alexander Chowdhury, M De Paolis Kaluza, Linfeng Zhao, Lawson Wong, and Rose
 678 Yu. Deep imitation learning for bimanual robotic manipulation. *Advances in neural information*
 679 *processing systems*, 33:2327–2337, 2020.
- 680 Chengyang Ying, Zhongkai Hao, Xinning Zhou, Hang Su, Songming Liu, Dong Yan, and Jun
 681 Zhu. Task aware dreamer for task generalization in reinforcement learning. *arXiv preprint*
 682 *arXiv:2303.05092*, 2023.
- 683
 684 Chengyang Ying, Zhongkai Hao, Xinning Zhou, Xuezhou Xu, Hang Su, Xingxing Zhang, and
 685 Jun Zhu. Peac: Unsupervised pre-training for cross-embodiment reinforcement learning. *arXiv*
 686 *preprint arXiv:2405.14073*, 2024.
- 687 Zhecheng Yuan, Tianming Wei, Shuiqi Cheng, Gu Zhang, Yuanpei Chen, and Huazhe Xu. Learning
 688 to manipulate anywhere: A visual generalizable framework for reinforcement learning. *arXiv*
 689 *preprint arXiv:2407.15815*, 2024.
- 690 Tony Z Zhao, Vikash Kumar, Sergey Levine, and Chelsea Finn. Learning fine-grained bimanual
 691 manipulation with low-cost hardware. *arXiv preprint arXiv:2304.13705*, 2023.
- 692
 693 Ziwen Zhuang, Zipeng Fu, Jianren Wang, Christopher Atkeson, Soeren Schwertfeger, Chelsea Finn,
 694 and Hang Zhao. Robot parkour learning. *arXiv preprint arXiv:2309.05665*, 2023.
- 695 Brianna Zitkovich, Tianhe Yu, Sichun Xu, Peng Xu, Ted Xiao, Fei Xia, Jialin Wu, Paul Wohlhart,
 696 Stefan Welker, Ayzaan Wahid, et al. Rt-2: Vision-language-action models transfer web knowledge
 697 to robotic control. In *Conference on Robot Learning*, pp. 2165–2183. PMLR, 2023.
- 698
 699
 700
 701

702 **A PROOFS**

704 **A.1 DETAILS AND PROOF OF THE LEMMA 1**

706 We follow the setting in Crammer & Mansour (2012). First, assume the hypothesis set of policies to
 707 grasp a fixed single point is \mathcal{H} and its VC dimension is d . When considering T tasks each represented
 708 by a different grasping position, we take the k -shared task classifier (\mathcal{H}_k, g) (Crammer & Mansour,
 709 2012). Here $\mathcal{H}_k = \{h_1, \dots, h_k\} \subseteq \mathcal{H}$ is a subset of \mathcal{H} and g maps each task $t \in \mathcal{T}$ to some $h_i \in \mathcal{H}_k$.
 710 Thus the k -shared task classifier hypothesis is defined as $\mathcal{F}_{\mathcal{H}, k} = \{f_{\mathcal{H}_k, g} : |\mathcal{H}_k| = k, \mathcal{H}_k \subseteq \mathcal{H}, g : \mathcal{T} \rightarrow K\}$, here $f_{\mathcal{H}_k, g}(\cdot, t) = h_{g(t)}(\cdot)$. Then Crammer & Mansour (2012) has shown that the VC
 711 dimension of $\mathcal{F}_{\mathcal{H}, k}$ is at most $\mathcal{O}(T \log k + kd \log(Tkd))$.

713 As we consider \mathcal{H} as the set of neural networks, previous works have shown that the VC dimension
 714 of multi-layer neural networks is around the parameters of the neural networks (Maass, 1994; Sontag
 715 et al., 1998). Thus $d \gg T$ in our setting and $\mathcal{O}(T \log k + kd \log(Tkd)) \approx \mathcal{O}(kd \log(Tkd))$.

716 Finally, we consider the task number T . Assume that grasping two points of which the distance
 717 below ϵ is similar, we need around $b^3 / \frac{4}{3}\pi\epsilon^3$ points for covering the grasping cube with size $b \times b \times b$.
 718 Thus the VC dimension is at most

$$\mathcal{O}(kd \log(Tkd)) = \mathcal{O}(kd \log(\frac{b^3}{\frac{4}{3}\pi\epsilon^3} kd)) = \mathcal{O}(kd \log(\frac{3b^3kd}{4\pi\epsilon^3})). \quad (5)$$

722 **A.2 PROOF OF THE LEMMA 2**

724 *Proof.* Firstly, we convert normalized coordinates to pixel coordinates:

$$\begin{aligned} u_{i\text{min(pixel)}} &= u_{i\text{min}} \times W_i \\ v_{i\text{min(pixel)}} &= v_{i\text{min}} \times H_i \\ u_{i\text{max(pixel)}} &= u_{i\text{max}} \times W_i \\ v_{i\text{max(pixel)}} &= v_{i\text{max}} \times H_i \end{aligned}$$

732 Then, we compute the center of the bounding box in pixel coordinates:

$$\begin{aligned} u_{i\text{center}} &= \frac{u_{i\text{min(pixel)}} + u_{i\text{max(pixel)}}}{2} \\ v_{i\text{center}} &= \frac{v_{i\text{min(pixel)}} + v_{i\text{max(pixel)}}}{2} \end{aligned}$$

738 These points represent the projections of the sphere's center onto the image planes.

739 Secondly, for each camera, we back-project the center point into a 3D viewing ray in camera coor-
 740 dinates:

$$\mathbf{d}_i = K_i^{-1} \begin{bmatrix} u_{i\text{center}} \\ v_{i\text{center}} \\ 1 \end{bmatrix}$$

744 This gives the direction vector \mathbf{d}_i in the camera coordinate system.

746 Therefore, we can express the sphere center in camera coordinates since the sphere's center lies
 747 somewhere along the viewing ray:

$$\mathbf{C}_{i,\text{cam}} = \lambda_i \mathbf{d}_i$$

749 where $\lambda_i > 0$ is an unknown scalar representing the distance along the ray from the camera center
 750 to the sphere's center.

751 Thirdly, we transform the sphere center from camera coordinates to world coordinates:

$$\mathbf{C} = R_i^\top \mathbf{C}_{i,\text{cam}} + \mathbf{t}_i = R_i^\top (\lambda_i \mathbf{d}_i) + \mathbf{t}_i$$

754 This must hold true for both cameras:

$$\mathbf{C} = R_1^\top (\lambda_1 \mathbf{d}_1) + \mathbf{t}_1 = R_2^\top (\lambda_2 \mathbf{d}_2) + \mathbf{t}_2$$

756 By equating the expressions for \mathbf{C} we get:
 757

$$R_1^\top(\lambda_1 \mathbf{d}_1) + \mathbf{t}_1 = R_2^\top(\lambda_2 \mathbf{d}_2) + \mathbf{t}_2$$

759 By rewriting we have:
 760

$$R_1^\top \mathbf{d}_1 \lambda_1 - R_2^\top \mathbf{d}_2 \lambda_2 = \mathbf{t}_2 - \mathbf{t}_1$$

761 Let's denote:
 762

$$\mathbf{a}_1 = R_1^\top \mathbf{d}_1$$

$$\mathbf{a}_2 = R_2^\top \mathbf{d}_2$$

$$\mathbf{b} = \mathbf{t}_2 - \mathbf{t}_1$$

763 So the equation becomes:
 764

$$\mathbf{a}_1 \lambda_1 - \mathbf{a}_2 \lambda_2 = \mathbf{b}$$

765 Note that this is a system of three linear equations with two unknowns λ_1 and λ_2 :
 766

$$\begin{cases} a_{1x}\lambda_1 - a_{2x}\lambda_2 = b_x \\ a_{1y}\lambda_1 - a_{2y}\lambda_2 = b_y \\ a_{1z}\lambda_1 - a_{2z}\lambda_2 = b_z \end{cases}$$

767 Since we have more equations than unknowns (overdetermined system), we can solve for λ_1 and λ_2
 768 using least squares estimation.
 769

770 Note that this can be written in matrix form:
 771

$$\begin{bmatrix} a_{1x} & -a_{2x} \\ a_{1y} & -a_{2y} \\ a_{1z} & -a_{2z} \end{bmatrix} \begin{bmatrix} \lambda_1 \\ \lambda_2 \end{bmatrix} = \begin{bmatrix} b_x \\ b_y \\ b_z \end{bmatrix}$$

772 Let A be the 3×2 matrix of coefficients, $\boldsymbol{\lambda}$ the vector of unknowns, and \mathbf{b} the vector of constants:
 773

$$A = \begin{bmatrix} a_{1x} & -a_{2x} \\ a_{1y} & -a_{2y} \\ a_{1z} & -a_{2z} \end{bmatrix}, \quad \boldsymbol{\lambda} = \begin{bmatrix} \lambda_1 \\ \lambda_2 \end{bmatrix}, \quad \mathbf{b} = \begin{bmatrix} b_x \\ b_y \\ b_z \end{bmatrix}$$

774 We can compute the least squares solution:
 775

$$\boldsymbol{\lambda} = (A^\top A)^{-1} A^\top \mathbf{b}$$

776 Once λ_1 and λ_2 are found, **C can be calculated using either camera's equation:**
 777

$$\mathbf{C} = R_1^\top(\lambda_1 \mathbf{d}_1) + \mathbf{t}_1$$

778 Alternatively, we compute both and average them for robustness:
 779

$$\mathbf{C} = \frac{1}{2} (R_1^\top(\lambda_1 \mathbf{d}_1) + \mathbf{t}_1 + R_2^\top(\lambda_2 \mathbf{d}_2) + \mathbf{t}_2)$$

780 Finally, since λ_i and λ_2 are found, we can compute the distance Z_i from the camera along the
 781 viewing direction \mathbf{d}_i :
 782

$$\mathbf{C}_{i,\text{cam}} = \lambda_i \mathbf{d}_i = Z_i \cdot \hat{\mathbf{d}}_i$$

783 where $\hat{\mathbf{d}}_i$ is normalized by:
 784

$$\hat{\mathbf{d}}_i = \frac{\mathbf{d}_i}{\|\mathbf{d}_i\|}$$

785 The projected radius of the sphere s_i (in pixels) is half the size of the bounding box width or height
 786 (assuming the sphere projects to a circle):
 787

$$s_i = \frac{w_i + h_i}{4}$$

788 where
 789

$$w_i = u_{i\text{max(pixel)}} - u_{i\text{min(pixel)}}$$

$$h_i = v_{i\text{max(pixel)}} - v_{i\text{min(pixel)}}$$

810 Consider similar triangles in the imaging geometry:

$$\frac{s_i}{f_i} = \frac{r}{Z_i}$$

814 **We can compute the radius of the sphere:**

$$r = \frac{s_i \cdot Z_i}{f_i}$$

818 Additionally, the solution is unique provided that:

- 820 • **The Cameras Are Not Aligned:** The direction vectors \mathbf{a}_1 and \mathbf{a}_2 are not colinear.
- 821 • **Non-Degenerate Configuration:** The cameras have different positions or orientations,
822 ensuring the lines of sight intersect at a single point.

824 Under these conditions, the least squares solution yields a unique λ , and thus unique \mathbf{C} and r .

825 \square

B ABLATION STUDY

830 To demonstrate the essential role of 3D spatial and 1D temporal information for spatial intelligence,
831 we perform an additional experiment focusing on **temporal variability**, in addition to the spatial
832 generalization tests in Sec. 4. This experiment includes an ablation study comparing models trained
833 on a few selected key timesteps with those trained on all timesteps in a full trajectory. To further
834 illustrate the robust inference capabilities achieved by the enhanced **policy generalization**, we test
835 the policy’s ability to handle significant uncertainty in the output of the visual model. During infer-
836 ence, we apply random masks and noise to the visual model’s bounding box outputs, allowing us to
837 evaluate the policy’s generalization ability under such conditions.

B.1 TRAINING WITH ONLY KEY STEPS.

841 To assess the impact of temporal information on policy effectiveness, we conduct an experiment
842 where the model is trained using only key steps from the trajectory. The specific key steps selected
843 were [0, 18, 20, 22, 70], chosen to represent pivotal moments in the trajectory for the grasping task:
844 0 corresponds to the initial state before the gripper starts approaching the apple, 70 represents the
845 final state when the robotic arm retracts, and steps 18 to 22 denote intermediate states where the
846 gripper makes contact with the apple and closes around it.

847 Table 2: Success Rates for Training with Only Key Steps

849 Experiment	850 Real Robot Success Rate	851 Simulation Success Rate
851 Training with Full Trajectory	90%	81.25%
852 Training with Key Steps	0%	4.17%

853 The results in Tab. 2 indicate a stark difference in performance between training with the full tra-
854 jectory and training with only key steps. Training with the full trajectory resulted in a success rate
855 of 90% on the real robot and 81.25% in simulation. In contrast, training with only key steps leads
856 to complete failure on the real robot (0% success rate) and a significantly reduced success rate of
857 4.17% in simulation. This outcome highlights that relying solely on key steps fails to provide the
858 temporal continuity necessary for effective spatial generalization. The policy’s inability to capture
859 sufficient context from isolated states results in poor action generation and overall task failure.

B.2 ROBUSTNESS AGAINST DETECTION FAILURE DURING INFERENCE.

861 During the inference phase, visual models such as YOLO-World may not always successfully iden-
862 tify objects, leading to significant uncertainty in visual input.



864
865
866
867
868
869
870 Figure 6: A case of detection failure. The task is to catch apples to a specified location in a normal
871 environment.
872

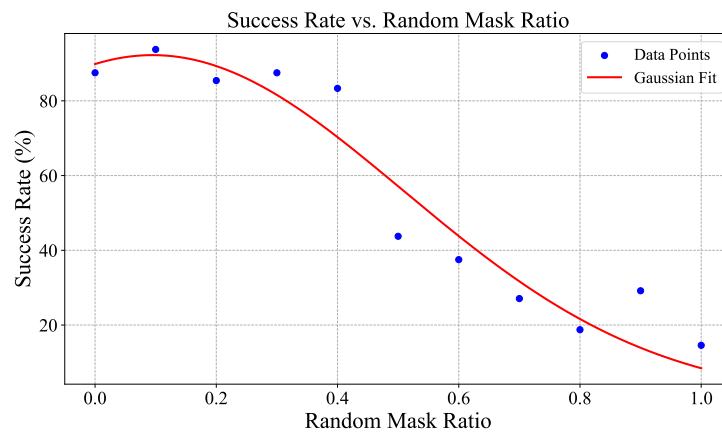


873
874
875
876
877
878 Figure 7: A case of detection failure. The task is to catch apples to a specified location in a flittering
879 light environment.
880
881

882 **Our policy still works well in situations where the visual model fails to detect.** For example,
883 visual models may fail to detect target objects when the robotic arm approaches the target, under
884 dim lighting conditions, or when there is partial occlusion of the target by the background (see
885 Figures 6 and 7). Especially, when using flickering and swaying point light sources in dimly lit
886 environments, the detection by visual models is particularly unstable. Such failures may occur at
887 any timestep during manipulation and may persist for several timesteps. Moreover, these failures
888 are unstable and unpredictable. For the same object placement, the occurrence of detection failures
889 during manipulation does not consistently happen or not happen at the same timestep.

890 Despite all those failures and instabilities in detecting bounding boxes, our model can still success-
891 fully and accurately accomplish the manipulation tasks.
892

893 To test our policy’s robustness against this visual uncertainty, we introduce masks that randomly
894 obscured bounding box input at varying ratios (0.0 to 1.0) during inference.
895



900
901
902
903
904
905
906
907
908
909
910 Figure 8: The relationship between random mask ratio and success rate. The fitted curve represents
911 a Gaussian function of $y = 92.23 \exp\left(-\frac{(x-0.09)^2}{2 \cdot 0.41^2}\right)$.
912
913

914 As shown in Fig. 8, the results reveal that the policy maintains a high success rate and generalization
915 capability when the mask ratio is below 0.4. As the mask ratio exceeds 0.4, the success rate signifi-
916 cantly declines, leading to consistent policy failures. Coincidentally, the random mask ratio we add
917 in the student policy training phase is 0.3. This trend reveals that our approach focusing on policy
generalizability can resist visual uncertainty up to 40% of the masking ratio. That is, even if 40%

918 of the visual information is lost, the policy still has good spatial generalizability. We fitted the data
 919 points with a Gaussian curve to represent this trend, defined by the equation:
 920

$$y(x) = a \cdot e^{-\frac{(x-b)^2}{2c^2}} \quad (6)$$

921 where a , b , and c are parameters that define the height, center, and width of the curve, respectively.
 922 This curve demonstrates that the policy is resilient up to moderate levels of visual masking (mask
 923 ratios up to 0.3), but performance degrades significantly as the masking ratio increases beyond 0.4.

924 This experiment validates that our policy can withstand moderate visual uncertainties during infer-
 925 ence, maintaining robust performance. This shows that our focus on policy generalization can easily
 926 cope with situations where the visual model has large uncertainty, leading to more robust manipula-
 927 tion. However, the steep decline in success rate for higher mask ratios highlights the importance of
 928 reliable visual input for effective spatial reasoning and task execution.

929 As to whether the random mask in the training phase gives some increase in the success rate of our
 930 policy, please refer to Sec. B.3.

931 B.3 RANDOM MASK DURING STUDENT POLICY TRAINING AFFECTS PERFORMANCE.

932 The uncertainty of visual detection in the real world is mentioned in the previous subsection, in order
 933 to demonstrate that random masking during training does favor the performance of the student pol-
 934 icy. Specifically, we compare the success rates of policies trained with and without a random mask
 935 ratio of 0.3 across five different spatial ranges. During training, we randomly mask out 0 to 30% of
 936 the bounding box information in each trajectory. This encourages the policy to adapt to scenarios
 937 where bounding box detection is incomplete or inaccurate. Table 3 demonstrated that in all range
 938 of spaces, the policy trained with random masks shows outstanding performance compared with
 939 one without masks. In addition, the policy shows better robustness in larger spatial ranges, where
 940 the variability and uncertainty of detection are more pronounced, highlighting the effectiveness of
 941 random masking in improving spatial adaptability and generalization.

942 Table 3: Comparison of Success Rates With and Without Random Mask

943 Spatial Range	944 Random Mask Ratio = 0.3	945 Without Random Mask
946 Fix Point	100.0%	100.0%
947 5 cm × 5 cm × 5 cm	83.33%	79.17%
948 10 cm × 10 cm × 10 cm	97.92%	64.58%
949 20 cm × 20 cm × 20 cm	87.5%	70.83%
950 Full Space (41 cm × 30 cm × 28 cm)	87.5%	68.75%

951 B.4 RANDOM NOISE IN BOUNDING BOXES DURING INFERENCE.

952 To further examine the policy’s robustness against visual uncertainty, we introduce random noise
 953 to the bounding boxes during inference. We tested noise ratios at increments of 0.01, 0.02, 0.05,
 954 0.1, 0.2, and 0.5. Fig. 9 illustrates the success rate as a function of noise ratio, where a monotonic
 955 decay fit highlights the policy’s performance trend. The results show that the policy maintains a
 956 high success rate at low noise ratios but experienced a significant decrease as noise levels increased.
 957 Since our normalized bounding box value ranges from 0 to 1, the policy still achieves a high success
 958 rate with a visual detection error of 0.05, demonstrating the robustness of the policy generalization
 959 to cope with visual uncertainty and visual sim2real gap.

960 Our experiments highlight that achieving spatial intelligence requires both continuous temporal in-
 961 formation and sufficient spatial data. The experiments in our main text demonstrate that spatial
 962 generalizability requires sufficient spatially varying data. The first ablation experiment shows that
 963 continuous temporal context is crucial for effective policy performance, while the second and third
 964 ablation experiments demonstrate that policy generalization can cope with notable visual uncer-
 965 tainty.

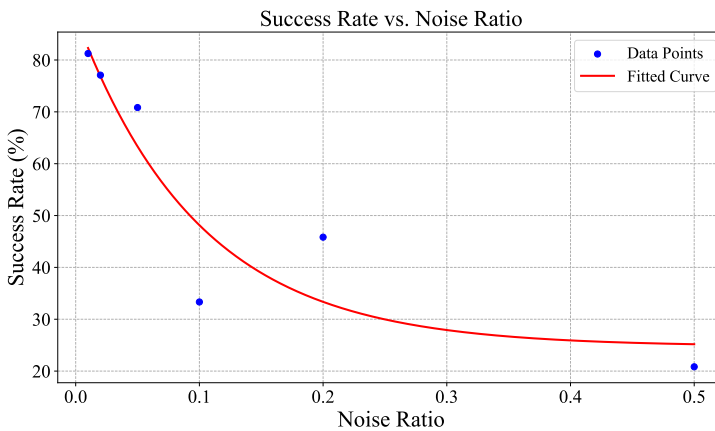


Figure 9: The relationship between random mask ratio and success rate. The fitted curve represents a exponential function of $y = 63.62 \exp(10.01x) + 24.75$.

C MORE REAL-WORLD EXPERIMENTS

To demonstrate the extensibility of our approach, we supplement four more real-world experiments: **Pour Water** (Figure 10), showcasing our approach’s extensibility to multi-object manipulation tasks; **Grab the handle of the cup** (Figure 11), illustrating our approach’s extensibility to the grasping of detailed parts of irregular objects; **Mid-Air** (Figure 12); and **Cluttered Table** at varying heights (Figure 13 and Figure 14).



Figure 10: **Task: Pour Water.** The policy grasps the left water bottle and pours water into the right cup, demonstrating the extensibility of our approach to complex tasks. By modifying the teacher policy in the simulator, this method can be extended to **more sophisticated tasks with more objects**.



Figure 11: **Task: Grab the handle of the cup.** More fine-grained detection can be achieved using models such as Liu et al. (2023), so that our policy can catch irregular objects, such as the handle of a cup. The first figure shows the recognition of the cup handle from the first-person view and the other figures show the task completion process from the third-person view.

D EXPERIMENTAL DETAILS

We test the success rate of student policy in both simulator and real world.

D.1 EVALUATION IN SIMULATION

We run large-scale experiments in the simulator to test the spatial generalization curve for each range and determine the minimum data amounts to achieve an optimal success rate. To align with real robot



Figure 12: **Task: Mid-Air.** Grasp the bottle lifted by hand and suspended in mid-air, then move it to the target position.



Figure 13: **Task: Cluttered Table.** Grasp the apple from a cluttered table with a height of 60 cm.

inference, we set the robot’s joints directly to target qpos instead of using environment stepping. We mark the trajectory as success if there is a step both reaching reward > 0.6 and quat reward > 1.4 . For each policy, we test 48 trajectories and record the final success rate. **The experiment consists of three rounds of tests with different seeds, each with 16 trajectories. In each round, the target random points are sampled from a uniform distribution.**

D.2 EXPERIMENT RESULT ANALYSIS

We discuss here the analysis of the results of spatial scaling law.

$$\text{data_volume} = 640.32 \cdot \text{spatial_volume}^{0.35} \quad (7)$$

By fitting the resulting data points, we observe that as the training data increases, the success rate of the policies quickly rises and eventually converges to an upper bound, which aligns well with the form of the Michaelis-Menten (Michaelis et al., 1913) equation:

$$\text{success_rate} = \frac{V_{\max} \times \text{num_traj}}{K_m + \text{num_traj}} \quad (8)$$

where V_{\max} represents the maximum achievable success rate, and K_m is the number of trajectories at which the success rate is half of V_{\max} . This equation captures the saturation-type growth observed in the policy performance.

Across different settings, the amount of data required to achieve an 80% success rate shows a power function as the data increases:

For the functional relationship between the amount of data required for spatial generalization and spatial volume, we explored two types of fits: a power law and a logarithmic function. The fitting results of power law is given by $y = a \cdot x^b = 640.32x^{0.35}$, while the logarithmic fit is $y = a \cdot \ln(b \cdot x) + c = 2095.51 \cdot \ln(0.3 \cdot x) - 642.93$. We found that the logarithmic fit becomes unreasonable as the spatial volume x approaches 0, where the required data, $y = a \cdot \ln(b \cdot x) + c = 2095.51 \cdot \ln(0.3 \cdot x) - 642.93$, tends to negative infinity, which is unrealistic since the amount of data cannot be negative. Furthermore, the fit results in a negative value at $x = 3.3$, where $bx = 1$ and $\log(bx) = 0$, leading to a required data amount of $a \log(bx) + c = -642.93$. In the long run (for larger spatial volumes), the power law fit better describes the relationship between the data required for spatial generalization and spatial volume. Fig. 15 shows the selected power law relationship, and Fig. 16 displays the logarithmic curve.

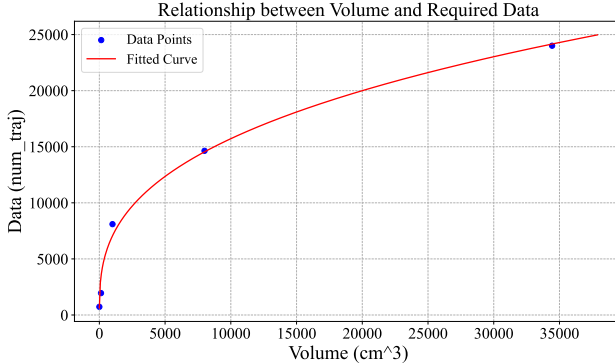
Figure 14: **Task: Cluttered Table.** Grasp the apple from a cluttered table with a height of 74.5 cm.

Figure 15: Demonstration of the power-rate relationship between spatial volume and data amounts needed to reach 80% success rate in the grasping task.

D.3 EVALUATION IN REAL WORLD

D.3.1 REAL-WORLD SUCCESS RATE

To verify our experiment results from the simulator, we evaluate our policy in the real robot. For each range, we choose the first optimal policy that achieves 80% success rate in simulator and evaluate with the real robot for 10 randomly chosen points.

Random Placement of Objects in Real-world Evaluation. To be more specific, we divide the maximum range, namely the full space ($41\text{cm} * 30\text{cm} * 28\text{cm}$), into three equal parts in height, two equal parts in width, and three equal parts in length, resulting in a total of $3 * 2 * 3 = 18$ equally sized spatial cuboid ranges at different positions. For each tested spatial range, ten different points are uniformly selected to test the robot’s manipulation success rate.

D.3.2 REAL-WORLD EXPERIMENT SETTINGS

To verify our methods, we evaluate our policy in the real robot. We evaluate the student policy which is trained on simulation data of full space ($41\text{cm} * 30\text{cm} * 28\text{cm}$) with the real robot.

Spatial Generalization. As illustrated in Fig. 5, we divide the spatial range horizontally into Left (L), Right (R), and Center (C), and vertically into Front (F) and Back (B), and randomly select points within these sections on different heights to test our policy². All these points are arbitrarily selected, which means that the target object has an equal chance of appearing at the center or the edge of the table, far from or close to the robot, in positions that require the robotic arm to reach upwards or downwards. We hope this approach reflects the spatial generalization of our policy comprehensively and honestly.

In addition to the verification of spatial generalization, we also test the ability of Object generalization and background generalization. The details of the experiment setting can be found in Tab. 4.

Object Generalization and Background Generalization. Furthermore, we have chosen objects of various shapes, sizes, and materials as target objects for testing, all of which were previously

²The table is an elevated table and can therefore be adjusted to any height.

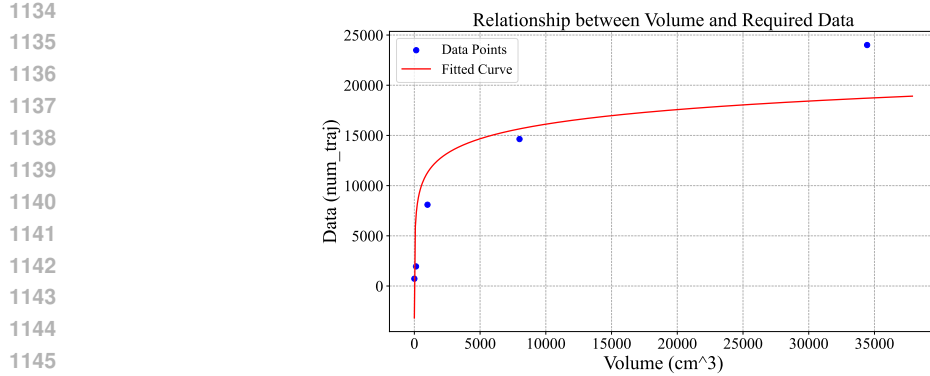


Figure 16: Demonstration of the logarithmic relationship between spatial volume and data amounts needed to reach 80% success rate in the grasping task.

unseen by our policy. To be more specific, during training, we only encountered apples with sizes of approximately (6.9cm – 7.4cm, 6.9cm – 7.4cm, 6.9cm – 7.4cm) in the XYZ direction, while the test target objects span a size range of (5.1cm – 7.0cm, 5.1cm – 9.7cm, 6.0cm – 22.7cm) in the XYZ direction. Additionally, although apples are roughly spherical, the target objects also include cylindrical and pyriform shapes. Moreover, the target objects encompass different materials such as glass and metal. All these objects serve to demonstrate our policy’s capability to generalize to varying shapes, sizes, and materials.

Table 4: Real-World Experiment Settings. Note that we use only the bounding boxes of the objects for both student policy training and inference. Bolded object sizes are never seen in training.

Generalization Type	Object Size (cm) of XYZ	Setting Description
Object in Simulation Data		
Apple (Domain Randomization)	(6.9-7.4, 6.9-7.4, 6.9-7.4)	Distribute uniformly in a configurable spatial volume
Object Generalization		
Yellow Pear	(6.5, 5.5, 10.7)	h4: Point Random, Minimal setting
Orange	(7.0, 6.7, 6.5)	h4: Point Random, Minimal setting
Steel Cup	(6.5, 9.7, 10.8)	h4: Point Random, Minimal setting
Tin Can	(5.1, 5.1, 7.2)	h4: Point Random, Minimal setting
Glass Beaker	(5.1, 5.1, 6.0)	h4: Point Random, Minimal setting
Background Generalization		
Apple	(7.2, 7.4, 6.9)	h4: Point Random, Orange tablecloth
Unseen Apple	(7.0, 7.5, 7.0)	h4: Point Random, Black tablecloth
Apple	(7.2, 7.4, 6.9)	h4: Point Random, Playing video
Apple	(7.2, 7.4, 6.9)	h4: Point Random, Dim light
Apple	(7.2, 7.4, 6.9)	h4: Point Random, Flittering light
Complex Generalization		
Unseen Apple, Unseen Table	(7.0, 7.5, 7.0)	Point Random, Table 2
Unseen Apple, Unseen Desk	(7.0, 7.5, 7.0)	Point Random, Multiple objects
Steel Cup, Unseen Desk	(6.5, 9.7, 10.8)	Point Random, Daily desktop
Plastic Bottle, Unseen Desk	(6.4, 6.4, 22.27)	Point Random, Daily desktop

The three camera images, as well as the entire trajectory of grasping, are schematized below in Figure 17:

E TEACHER-STUDENT TRAINING DETAILS

For ease of understanding, Alg. 1 is the pseudo algorithm for the ManiBox method.

1188
 1189
 1190
 1191
 1192
 1193
 1194
 1195
 1196

Algorithm 1 Training and Deployment Algorithm of ManiBox

1197
Require: Simulator environment Sim , Real robot $Robot$
 1199 **Require:** Proximal Policy Optimization (PPO) for training teacher policy
 1200 **Require:** Bounding box extractor $BBoxExtractor$
 1201 **Require:** Maximum dataset size N_{max} , reward function R , domain randomization module DR

1202 1: **Stage 1: Teacher Policy Training**
 1203 2: Initialize teacher policy π_β with random weights
 1204 3: Set Sim environment with reward function R and domain randomization module DR
 1205 4: **while** not converged **do**
 1206 5: Collect trajectory data \mathcal{D}_T in Sim using π_β
 1207 6: Update π_β using PPO with \mathcal{D}_T
 1208 7: **end while**

1209
 1210 8: **Stage 2: Simulation Data Generation**
 1211 9: Initialize dataset $\mathcal{D}_S = \emptyset$
 1212 10: **while** $|\mathcal{D}_S| < N_{max}$ **do**
 1213 11: Reset Sim environment
 1214 12: Apply domain randomization DR to environment
 1215 13: Generate trajectory $\tau = \{(o_t^{rob}, a_t, r_t)\}_{t=1}^T$ using π_β
 1216 14: Extract bounding boxes $\{o_t^{vis}\}_{t=1}^T$ using $BBoxExtractor$
 1217 15: Store $\{(o_t^{vis}, o_t^{rob}, a_t)\}_{t=1}^T$ in \mathcal{D}_S
 1218 16: **end while**

1219
 1220 17: **Stage 3: Student Policy Training**
 1221 18: Initialize student policy π_θ with random weights
 1222 19: **while** not converged **do**
 1223 20: Sample trajectory $\tau = \{(o_t^{vis}, o_t^{rob}, a_t)\}_{t=1}^T$ from \mathcal{D}_S
 1224 21: Randomly mask some o_t^{vis} to simulate detection failures
 1225 22: Update $\pi_\theta(o_{\leq t}^{vis}, o_{\leq t}^{rob})$ using the masked τ
 1226 23: **end while**

1227
 1228 24: **Stage 4: Real-World Deployment**
 1229 25: $t \leftarrow 0$
 1230 26: **while** not terminated **do**
 1231 27: Extract real-world bounding boxes o_t^{vis} using $BBoxExtractor$
 1232 28: Compute action $a_t \sim \pi_\theta(o_{\leq t}^{vis}, o_{\leq t}^{rob})$
 1233 29: Execute action a_t on $Robot$
 1234 30: $t \leftarrow t + 1$
 1235 31: **end while**

1236
 1237
 1238
 1239
 1240
 1241



Figure 17: Pictures of the entire trajectory of grasping, including perspective and three camera views.

E.1 TEACHER POLICY DETAILS

We train our teacher policy using PPO with 8,192 parallel environments in Isaac Lab (Mittal et al., 2023). With a carefully designed reward function and applied PPO techniques, the training is completed in around 40 minutes, reaching approximately 2,000 training iterations. **The task involves training a robot to grasp an apple randomly placed on a liftable table and transport it to a designated target position (Figure 18).**



Figure 18: The simulation environment consists of a room with a table, an apple, and a robot. The task is for the robot to grasp the apple and place it in a specified location.

The advantages of using a teacher policy instead of direct visual RL training can be summarized in three key aspects. First, the teacher policy relies solely on robot and object information as input, significantly reducing the dimensionality of the state space. Second, the incorporation of privileged information and tailored reward functions for critical steps offers more focused guidance during training, thereby narrowing the exploration space. Lastly, visual RL suffers from limited parallelizability, which results in lower overall training efficiency.

E.1.1 SIMULATION SCENARIO SETUP

The environment is built based on the lift task in Isaac Lab. During training, the scene consists of a table, an apple, and a robot. The robot is initialized at a fixed starting position at the beginning of each episode. The apple's size, as well as its x,y position, are uniformly randomized across environments, while the height of the table is also uniformly randomized. The target position, however, remains fixed throughout all training episodes. Key steps captured from three camera perspectives

1296
1297
1298
1299
1300
1301
1302
1303
1304
1305
1306
1307
1308
1309
1310
1311
1312
1313
1314
1315
1316
1317
1318
1319
1320
1321
1322
1323
1324
1325
1326
1327
1328
1329
1330
1331
1332
1333
1334
1335
1336
1337
1338
1339
1340
1341
1342
1343
1344
1345
1346
1347
1348
1349
are shown in Figures 19, 20, and 21. To support future extensions to more complex tasks, such as obstacle avoidance during grasping, we represent the robot's behavior with a 30Hz trajectory. Each environment in the simulator is evenly spaced to prevent interference between different training instances. Further details on the randomized ranges can be found in Table 5.



Figure 19: Key steps of grasping in simulation in cam_high view.



Figure 20: Key steps of grasping in simulation in cam_left_wrist view.



Figure 21: Key steps of grasping in simulation in cam_right_wrist view.

Table 5: Environment Randomization Parameters

Spatial Range	Table Height (z)	Apple X Position	Apple Y Position
Fix Point	(-0.00, 0.00)	(-0.0, 0.0)	(-0.0, 0.0)
5 cm × 5 cm × 5 cm	(-0.025, 0.025)	(-0.025, 0.025)	(-0.025, 0.025)
10 cm × 10 cm × 10 cm	(-0.07, 0.03)	(-0.05, 0.05)	(-0.05, 0.05)
20 cm × 20 cm × 20 cm	(-0.1, 0.1)	(-0.1, 0.1)	(-0.05, 0.15)
Full Space (41 cm × 30 cm × 28 cm)	(-0.13, 0.15)	(-0.22, 0.08)	(-0.05, 0.36)
Apple 3D Scale Range	((0.77, 0.82), (0.77, 0.82), (0.77, 0.82))		

E.1.2 DETAILS OF OBSERVATION AND ACTION

We provide detailed information about the observations and actions used in training the teacher policy for the multi-environment object-grasping manipulation task:

- **Observations:**
 - Contact forces (24-dimensional)
 - Joint position (8-dimensional)
 - Joint velocity (8-dimensional)
 - Object position (3-dimensional)
 - Target location (7-dimensional)

- 1350 – Last action (8-dimensional)
 1351 • **Actions:**
 1352 – Joint Position (8-dimensional) (We choose position control. The action is the expected
 1353 joint position for the next timestep.)
 1354

1355 E.1.3 IMPLEMENTATION OF PPO
 1356

1357 Our PPO implementation is built on `rsl.rl`, and leverages several techniques to improve stability and
 1358 performance. Key components and their settings are summarized in Table 6.
 1359

1360 Table 6: PPO Parameter Settings
 1361

Techniques	Parameter	Value
Clipped Surrogate Objective	clip_param	0.2
Value Function Clipping	use_clipped_value_loss	True
Value Loss Coefficient	value_loss_coeff	1.0
Adaptive KL Penalty	desired_kl	0.01
Entropy Regularization	entropy_coeff	0.01
Generalized Advantage Estimation (GAE)	gamma	0.99
	lam	0.95
Gradient Clipping	max_grad_norm	1.0
Learning Rate	learning_rate	0.001
Mini-Batch	num_mini_batches	4
Learning Epochs	num_learning_epochs	5
Schedule	schedule	adaptive
Empirical Normalization	empirical_normalization	True

1375 E.1.4 REWARD FUNCTION DESIGN
 1376

1378 To ensure the policy achieves the desired grasping behavior on our robot, we design a reward function
 1379 that reflects the task’s objectives. As grasping is complicated, it can be divided into a multi-stage
 1380 reward function: first reaching the object, then closing the jaws, then picking up the object, and fi-
 1381 nally retracting the robotic arm to a specified position. Definitions of different part of our reward
 1382 function for the specific object-grasp task are stated as follows:
 1383

1384 • Fingers Open

$$R_{\text{fingers_open}} = \tanh\left(\frac{\|\mathbf{p}_{\text{object}} - \mathbf{p}_{\text{ee}}\|_2}{\sigma}\right) \cdot \sum_{i=1}^2 \text{finger_pos}[i]$$

1388 where $\mathbf{p}_{\text{object}}$ represents the position of the object in world coordinates. \mathbf{p}_{ee} represents the
 1389 position of the end-effector in world coordinates. finger_pos represents the joint positions
 1390 of the robot’s fingers. $\sigma = 0.1$ is a scaling factor for distance normalization.
 1391

1392 • Reaching Object

$$R_{\text{reaching_object}} = \left(1 - \tanh\left(\frac{\|\mathbf{p}_{\text{object}} - \mathbf{p}_{\text{ee}}\|_2}{\sigma}\right)\right) + \left(1 - \tanh\left(\frac{\|\mathbf{p}_{\text{object}} - \mathbf{p}_{\text{ee}}\|_2}{\sigma/4}\right)\right)$$

1395 where $\mathbf{p}_{\text{object}}$ represents the position of the object in world coordinates. \mathbf{p}_{ee} represents the
 1396 position of the end-effector in world coordinates. $\sigma = 0.2$ is a scaling factor for distance
 1397 normalization.
 1398

1399 • Object Goal Tracking

$$R_{\text{goal_tracking}} = \mathbb{1}(\mathbf{p}_{\text{object},z} > z_{\text{init}} + h_{\text{min}}) \cdot \left(1 - \tanh\left(\frac{\|\mathbf{p}_{\text{goal}} - \mathbf{p}_{\text{object}}\|_2}{\sigma}\right)\right)$$

1402 where \mathbf{p}_{goal} represents the target position of the object in world coordinates. $\mathbf{p}_{\text{object}}$
 1403 represents the position of the object in world coordinates. $\mathbf{p}_{\text{object},z}$ represents the z -
 coordinate (height) of the object in world coordinates. z_{init} is the initial height of the object.
 1401

1404 $h_{\min} = 0.02$ is the minimal height above the initial height required to achieve the goal.
 1405 $\sigma = 0.3$ is a scaling factor for distance normalization.

- **Object Goal Tracking (Fine-Grained)**

$$1408 \quad R_{\text{goal_tracking_fine}} = \mathbb{1}(\mathbf{p}_{\text{object},z} > z_{\text{init}} + h_{\min}) \cdot \left(1 - \tanh \left(\frac{\|\mathbf{p}_{\text{goal}} - \mathbf{p}_{\text{object}}\|_2}{\sigma_{\text{fine}}} \right) \right)$$

1410 where \mathbf{p}_{goal} represents the target position of the object in world coordinates. $\mathbf{p}_{\text{object}}$ represents the position of the object in world coordinates. z_{init} is the initial height of the object.
 1411 $h_{\min} = 0.02$ is the minimal height above the initial height required to achieve the goal.
 1412 $\sigma_{\text{fine}} = 0.05$ provides finer scaling for precise tracking.

- **Action Rate Penalty**

$$1415 \quad R_{\text{action_rate}} = -\|\mathbf{a}_t - \mathbf{a}_{t-1}\|_2^2$$

1416 where \mathbf{a}_t represents the action at the current time step. \mathbf{a}_{t-1} represents the action at the
 1417 previous time step.

- **Joint Velocity Penalty**

$$1419 \quad R_{\text{joint_vel}} = -\sum_{i \in \text{joint_ids}} \dot{q}_i^2$$

1420 where \dot{q}_i represents the joint velocity of the i -th joint. joint_ids is the set of joint indices to
 1421 penalize.

- **Contact Forces**

$$1425 \quad R_{\text{contact_forces}} = \mathbb{1} \left(\frac{\text{finger_dist}}{4} < \text{proj_len} < \frac{\text{finger_dist}}{1.25} + 0.2 \right) \cdot \left(1.2 - \tanh \left(\frac{\text{object_dist}}{0.2} \right) \right)$$

$$1428 \quad \cdot \mathbb{1} (\|\mathbf{p}_{\text{object}} - \mathbf{p}_{\text{top}}\| < 0.1) \cdot \left(1 - \tanh \left(\frac{\|\mathbf{org_vec} - \mathbf{y}\|}{0.3} \right) \right)$$

1429 where $\mathbf{p}_{\text{top}}, \mathbf{p}_{\text{bottom}}, \mathbf{p}_{\text{left}}, \mathbf{p}_{\text{right}}$ are the positions of the robot's end-effector fingers (top, bottom, left, right) in world coordinates. $\mathbf{p}_{\text{object}}$ is the position of the object in world coordinates. $\mathbf{org_vec} = \mathbf{p}_{\text{left}} - \mathbf{p}_{\text{right}}$ is the vector between the left and right fingers, rotated into the object's local frame. $\mathbf{y} = [0, 1, 0]$ is the unit vector along the y-axis in the object's local frame. $\text{finger_dist} = \|\mathbf{p}_{\text{left}} - \mathbf{p}_{\text{right}}\|_2$ is the distance between the left and right fingers. $\text{proj_len} = \frac{(\mathbf{p}_{\text{object}} - \mathbf{p}_{\text{left}}) \cdot (\mathbf{p}_{\text{right}} - \mathbf{p}_{\text{left}})}{\text{finger_dist}}$ is the projection of the object's position onto the vector between the left and right fingers. $\text{object_dist} = \frac{\|\mathbf{p}_{\text{object}} - \mathbf{p}_{\text{bottom}} \times (\mathbf{p}_{\text{top}} - \mathbf{p}_{\text{bottom}})\|}{0.11}$ is the perpendicular distance from the object to the line formed by the bottom and top fingers.

- **Close Fingers**

$$1440 \quad R_{\text{close_fingers}} = \mathbb{1}(\text{grasp_force} > 0.5) \cdot \left(1 - \tanh \left(\frac{\sum_{i=1}^2 \text{finger_pos}[i]}{0.1} \right) \right)$$

1443 where grasp_force represents the force exerted by the fingers on the object. finger_pos
 1444 represents the joint positions of the robot's fingers.

- **Lift End Effector (EE)**

$$1447 \quad R_{\text{lift_ee}} = \frac{\text{clamp}(\mathbf{p}_{\text{ee},z} - 0.6, 0.0, 0.3)}{0.3} \cdot \mathbb{1}(\text{grasp_force} > 0.5)$$

1449 where $\mathbf{p}_{\text{ee},z}$ represents the height of the end-effector above the ground.

- **Lift Object**

$$1452 \quad R_{\text{lift_object}} = \mathbb{1}(\mathbf{p}_{\text{object},z} > z_{\text{init}} + h_{\min}) \cdot \frac{\text{clamp}(\mathbf{p}_{\text{object},z} - z_{\text{init}} - h_{\min}, 0.0, 0.2)}{0.2}$$

1454 where $\mathbf{p}_{\text{object},z}$ represents the height of the object above the ground. z_{init} is the initial height
 1455 of the object. $h_{\min} = 0.02$ is the minimal height above the initial height required to achieve
 1456 the goal.

1457 Details of our weight design for the reward function can be found in Table 7

Table 7: Reward Function Design

Reward Term	Weight
Fingers Open	5.0
Reaching Object	15.0
Object Goal Tracking	80.0
Object Goal Tracking (Fine-Grained)	70.0
Action Rate Penalty	-1e-4
Joint Velocity Penalty	-1e-4
Contact Forces	10
Close Fingers	100
Lift End Effector (EE)	20
Lift Object	100

E.2 DATA GENERATION DETAILS

In data generation, as shown in Fig. 2, we feed the images from the n_{cam} first-person cameras of the robot to YOLO-World at each timestep to detect the n_{obj} target objects to be manipulated, thus obtaining $n_{cam} * n_{obj}$ bounding boxes. Then we normalize the bounding box, concatenate them, and obtain a vector \mathbf{o} of dimension $4 * n_{cam} * n_{obj}$ as the visual feature input for the control policy. We then store the visual features $\mathbf{o}_t^{\text{vis}}$, all joint positions of the robot $\mathbf{o}_t^{\text{rob}}$, and actions a_t for each step in the form of trajectories.

To reduce visual interference between parallel environments and minimize the sim-to-real gap, we incorporate a white room during data collection. [The room is designed to be spacious enough to accommodate the maximum working space, including robot, table, and apple.](#) Three RGB-D cameras³, calibrated with intrinsic and extrinsic parameters matching those of the real robot, capture visual information. During inference, the images from these cameras are processed by YOLO-World to generate object bounding boxes.

Table 8: Camera Parameters

Camera	Link	Image Shape and Type
cam_high	fr_link6	Shape: [480, 640, 4] RGB, Range: 0-255 (torch.uint8)
cam_left_wrist	fl_link6	Shape: [480, 640, 4] RGB, Range: 0-255 (torch.uint8)
cam_right_wrist	fr_link6	Shape: [480, 640, 4] RGB, Range: 0-255 (torch.uint8)

Given the high memory demands of image data, we run 16 parallel environments on a single GPU⁴ for data generation, achieving up to 36k successful trajectories per day. For ACT training, these trajectories are subsequently stored in an HDF5 data structure⁵ (see Table 9). In our approach, we convert images to bounding boxes using YOLO-World and store the results in a dictionary format. Each trajectory consists of multiple steps, with each step containing bbox, qpos, and action data.

E.3 STUDENT POLICY DETAILS

We use RNN and ACT to train our student policy. The details of training parameters can be found in Table 10 and Table 11.

³But we only use RGB information.

⁴For some 24 GB GPU.

⁵Video-based dataset

Table 9: HDF5 Data Structure

Group/Attribute	Dataset/Attribute Name	Description
Root Attributes	sim	Boolean indicating simulation (False)
	compress	Compression flag from ‘CollectEpsBuf’
Datasets	action	Array of actions taken
	reward	Array of rewards received
	base_action	Array of base actions
	base_action_t265	(Optional) Base actions from T265 sensor
Observations: states	qpos	Array of joint positions
	qvel	Array of joint velocities
	effort	Array of joint efforts
Observations: images	cam_high	Byte-encoded images from ‘cam_high’
	cam_left_wrist	Byte-encoded images from ‘cam_left_wrist’
	cam_right_wrist	Byte-encoded images from ‘cam_right_wrist’

Table 10: RNN Training Parameters

Parameter	Value
lr	0.002
lr_backbone	7e-05
epochs	50
warmup_ratio	0.1
use_scheduler	cos
weight_decay	0.0001
loss_function	l1
hidden_dim	512
rnn_layers	3
rnn_hidden_dim	512
actor_hidden_dim	512
policy_class	RNN
gradient_accumulation_steps	1
random_mask_ratio	0.3

E.4 SIM2REAL TECHNIQUE

We employ the student policy for sim-to-real transfer, where the inputs to the policy included proprioception o_t^{rob} which consists of joint positions, and the visual input o_t^{vis} , represented by bounding boxes. The output action is the desired joint position for the next step. Thus, the primary sim-to-real gaps exist in the joint position and bounding box dimensions.

For joint positions, we develop a real-to-sim code that maps the joint positions obtained from teleoperation on a real-world robot to a simulated robot. We evaluate whether the actions performed at specific target positions were consistent between the real-world and simulated environments. For example, when teleoperating to grasp an apple at a precisely measured location, both the real-world and simulated apples are set at the same coordinates. We used the main arm of the real-world robot to observe whether the simulated robot could successfully grasp the apple.

Special handling is required for the gripper, as there are discrepancies between the URDF model of the gripper and its real-world counterpart. In the simulation, the gripper has two joints, while in reality, it functions as a single joint, leading to differences in value interpretation. To address this, we collect 10 data sets for fitting and utilize function interpolation to map the simulated gripper joint positions to those of the real-world gripper. This approach ensures that the state space and action space are aligned between the simulation and the real environment.

The sim-to-real gap for the bounding boxes corresponds to the image sim-to-real gap. We perform hand-eye calibration on the camera to ensure that the cameras in both the simulation and the real-

1566

Table 11: ACT Training Parameters

1567

1568

1569

1570

1571

1572

1573

1574

1575

1576

1577

1578

1579

1580

1581

1582

1583

1584

1585

1586

1587

world robot are approximately aligned. For finer adjustments, we select a specific point in front of the robot and a specific-sized object, observing the bounding boxes obtained from both the simulator and the real-world camera. Since we use bounding boxes, other factors such as lighting and background variations in the sim-to-real gap are not a concern. Ultimately, this method of adjustment ensures that the intrinsic and extrinsic parameters of the camera are consistent between the simulation and the real-world environment.

1593

Other methods to ensure successful Sim2Real, such as domain randomization, are described in the previous section (Sec. 3.2).

1594

1595

1596

F HARDWARE DETAILS

1597

1598

The robot is equipped with a dual-arm design, providing a total of 14 degrees of freedom (DoF), with 7 DoF per arm for versatile movement. Each arm has a maximum valid payload of 1500g, and the gripper has a range of up to 80mm, allowing the robot to perform a variety of grasping and manipulation tasks efficiently. The detailed hardware information and an image of the robot can be found in Figure 22 and Table 12.

1599

1600

1601

1602

1603

Parameter	Value
Size	1080 × 700 × 1140
Arm weight	4.2 kg
Arm Payload	3000 g (peak) 1500 g (valid)
Arm reach	600 mm
Arm repeatability	1 mm
Arm working radius	653 mm
Joint motion range	J1: $\pm 154^\circ$, J2: $0^\circ \sim 165^\circ$ J3: $-175^\circ \sim 0^\circ$, J4: $\pm 106^\circ$ J5: $\pm 75^\circ$, J6: $\pm 100^\circ$
Gripper range	0-80 mm
Gripper max force	10 NM
DoF	$7 \times 2 = 14$

1618

1619

Table 12: Technical specifications.



Figure 22: Hardware features.

G LIMITATIONS AND DISCUSSIONS

One of the limitations of ManiBox is that the accuracy of the obtained bounding box depends on the capability of the preceding visual model. As the YOLO-World sometimes may not be able to accurately partition the bounding box, ManiBox may grasp the wrong positions due to the wrong input bounding box. Also, the bounding box is mainly for objects with convex shapes and may be insufficient for handling flexible objects and fluids. In the future, a promising direction is to apply more powerful visual models like Grounding DINO and capture more semantic visual signals like segmentation via SAM in ManiBox to improve its ability. Also, for some complicated manipulation tasks like folding up clothes, directly training an RL teacher agent in the simulator may be difficult. Thus how to utilize human demonstration or state machine to get the expert teacher agent is also worth researching.

1620
16211622 One of the limitations of ManiBox is that the accuracy of the obtained bounding box depends on
1623 the capability of the preceding visual model. As the YOLO-World sometimes may not be able to
1624 accurately partition the bounding box, ManiBox may grasp the wrong positions due to the wrong
1625 input bounding box. Also, the bounding box is mainly for objects with convex shapes and may be
1626 insufficient for handling flexible objects and fluids. In the future, a promising direction is to apply
1627 more powerful visual models like Grounding DINO and capture more semantic visual signals like
1628 segmentation via SAM in ManiBox to improve its ability. Also, for some complicated manipulation
1629 tasks like folding up clothes, directly training an RL teacher agent in the simulator may be difficult.
1630 Thus how to utilize human demonstration or state machine to get the expert teacher agent is also
1631 worth researching.

1632

1633

1634

1635

1636

1637

1638

1639

1640

1641

1642

1643

1644

1645

1646

1647

1648

1649

1650

1651

1652

1653

1654

1655

1656

1657

1658

1659

1660

1661

1662

1663

1664

1665

1666

1667

1668

1669

1670

1671

1672

1673